Development of The Online Event Selection Program for The BELLE Experiment

HIGUCHI Takeo
Department of Physics, Faculty of Science, The University of Tokyo

12 Jan 1999

Abstract

In this thesis, the development of the fast event reconstruction program for the BELLE experiment is described. The event reconstruction monitors detector performance, rejects backgrounds and classifies the events. The track reconstruction program is developed to realize these goals. The event reconstruction speed is estimated to be 433μs, which can keep up with the maximum DAQ rate of 500Hz.

Contents

List of Tables

List of Figures

Chapter 1

Introduction

To answer why the matter dominates over the anti-matter in our universe searching for the origin of the CP violation is essential. Kobayashi and Maskawa offered a hypothesis that the extension of the Cabbibo matrix may gives the origin of the CP violation [1]. To test the validity of their hypothesis the BELLE [2] experiment has begun at KEK. In the BELLE experiment, the measurement on the CP violation is performed in the B meson system produced by $\Upsilon(4S)$ which is the resonance state of the $b\overline{b}$.
The KEKB collider is an $e^+\,e^-$ collider. The maximum luminosity is about $10^{34}\mathrm{cm}^{-2}\mathrm{s}^{-1}$, which corresponds to the yield of 1.0×10^6 $\Upsilon(4S)$ per day. In addition to the signal events of $\Upsilon(4S)$ we have $\tau^+\,\tau^-$ events, or $c\,\overline{c}$ events which also give a chance of an interesting physics study. In total, the rate of the events of interest becomes about 100Hz. In addition, we also have background events. The dominant sources of the background include the spent electron, synchrotron radiation, beam gas scattering and the electronics noise, and the physics processes such as $\gamma\,\gamma$ events, Bhabha events, and $\mu^+\,\mu^-$ process. The estimated background rate is about 100Hz.

The triggered events (including physics and background) are taken by the data acquisition system and first sent to the online computer farm. After the preprocessing of the data, they are sent to the computer center which is located 3km apart from the experimental hall via optical fiber cable and then written onto tapes. The data on the tapes are processed on the offline computer farm and reduced to the data summary tapes.

We do not want to store the background events which only waste the data storage space and the CPU time for the creation of the summarized event tapes. Background rejection is essential in as earlier step as possible. One of the major roles of the online computer farm is the background rejection. The online event reconstruction processing must be fast enough to keep up with max DAQ rate.

In this thesis, the track and momentum reconstruction in fast performance is

described [3]. And by applying the developed tracker, the simulation study about the performance of the event selection on the online computer farm is described.

Chapter 2

CP Violation

2.1 Definitions of P and C

To see the CP conservation, let us consider the weak decay:

$$\pi^+ \to \mu^+ \nu_\mu. \tag{2.1}$$

The helicity of the neutrinos are $-1/2$, where the helicity h is defined by

$$h \equiv \boldsymbol{s} \cdot \frac{\boldsymbol{q}}{|\boldsymbol{q}|}. \tag{2.2}$$

In eq. (2.2), $\boldsymbol{q}$ is the momentum and $\boldsymbol{s}$ is the spin. The neutrinos have the spin which is parallel to its momentum.

Here, let us apply the parity transformation to decay mode of (2.1). The parity transformation P is defined by

$$(x, y, z) \stackrel{P}{\to} (-x, -y, -z). \tag{2.3}$$

The application yields the helicity $+1/2$ ν_μ, because $P\boldsymbol{q}$ is $-\boldsymbol{q}$ while $P\boldsymbol{s}$ is $\boldsymbol{s}$. However, neutrinos with helicity $+1/2$ are not found in our universe. Therefore, we can conclude that the P transformation is violated in the decay of (2.1).

Next, let us apply the charge conjugation transformation C to (2.1). By the C transformation, (2.1) is transformed to

$$\pi^- \to \mu^- \overline{\nu}_\mu. \tag{2.4}$$

The decay mode of (2.4) implies that $\overline{\nu}_\mu$has the helicity of $-1/2$ because we are not applying the P transformation. However, as same as the ν_μ, anti-neutrinos with the helicity $-1/2$ are not also discovered. Therefore, we can conclude that the C transformation is also violated in the decay of (2.1).

In stead of C and P are violated, CP is conserved in the decay of (2.1). CP transformation of (2.1) yields the decay mode of (2.4) with the $\overline{\nu}_\mu$of helicity $+1/2$. This satisfies the experimental results. Long time until 1964, CP conservation is convinced even in the weak interaction.

2.2 Discovery of CP Violation

The first discovery of the CP invariance was made in the K meson system.
There were the problem that both K^0 and $\overline{K}^0$ are seemed to have two different lifetimes.
The given solution for this problem was that both K^0 and $\overline{K}^0$ are the state of linear combination of two different K mesons — K_S^0 and K_L^0.
K_S^0 is a short living K which decays in the decay mode of $K_S^0 \to 2\pi$, and K_L^0 is a long living K which decays in the decay mode of $K_L^0 \to 3\pi$. Since the CP value of final state 2π is +1, and that of 3π is -1, K_S^0 is assumed as a CP +1 particle, and K_L^0 was assumed as a parity -1 particle.
With the choice of the phase of K^0 and $\overline{K}^0$ as

$$CP\left|K^0\right\rangle = \left|\overline{K}^0\right\rangle \tag{2.5}$$

$$CP\left|\overline{K}^0\right\rangle = \left|K^0\right\rangle, \tag{2.6}$$

K_L^0 and K_S^0 can be represented as

$$\left|K_L^0\right\rangle = \frac{1}{\sqrt{2}}\left(\left|K^0\right\rangle - \left|\overline{K}^0\right\rangle\right) \tag{2.7}$$

$$\left|K_S^0\right\rangle = \frac{1}{\sqrt{2}}\left(\left|\overline{K}^0\right\rangle + \left|K^0\right\rangle\right). \tag{2.8}$$

These representation are consistent to the eigenvalues of their final state.
However, in 1964, Fitch group found that eq. (2.8) was an approximation by showing [4] the decay of

$$K_L^0 \to \pi^+\,\pi^-. \tag{2.9}$$

They studied this mode with using the fact that K_L^0 has 500th as long lifetime as K_S^0. After the long enough time not to be affected from the K_S^0 decay, they proved the existence of decay mode of (2.9).
And their result concludes that the CP invariance was violated.

2.3 Origin of the CP Violation

Let us see the theoretical origin of the CP violation.

The leptons and quarks interact with the V-A type current:

$$\begin{aligned} \nu_e &\longleftrightarrow e^- \\ \nu_\mu &\longleftrightarrow \mu^- \\ u &\longleftrightarrow d. \end{aligned} \tag{2.10}$$

Each fermion is the mass eigenstate itself and it seems to be also the eigenstate of the weak interaction. They form a doublet of the weak interaction.
However we know the weak decay of

$$K^+ \to \mu^+ \nu_\mu. \tag{2.11}$$

Because the components of K^+ are u and $\overline{s}$ quark, there must exist the weak interaction between

$$u \longleftrightarrow s. \tag{2.12}$$

It violates the doublet theory of the weak interaction. The solution for this problem was given by Cabbibo in 1963 [5]. His idea is that the mass eigenstate is not the weak interaction eigenstate, and he wrote the eigenstates of the weak interaction by the linear combination of the mass eigenstate:

$$\begin{pmatrix} d' \\ s' \end{pmatrix} = \begin{pmatrix} \cos\theta_{\rm C} & \sin\theta_{\rm C} \\ -\sin\theta_{\rm C} & \cos\theta_{\rm C} \end{pmatrix} \begin{pmatrix} d \\ s \end{pmatrix}. \tag{2.13}$$

The quarks with q' is the eigenstates of the weak interaction. The "mixing angle" $\theta_{\rm C}$ is known as Cabbibo angle.
Kobayashi and Maskawa expanded Cabbibo's theory. They offered a hypothesis of three-generation quarks and showed its necessity for description of the CP violation.
For the following discussion, we define the elements of Cabbibo-Kobayashi-Maskawa matrix as in eq. (2.14).

$$V_{KM} \equiv \begin{pmatrix} V_{ud} & V_{us} & V_{ub} \\ V_{cd} & V_{cs} & V_{cb} \\ V_{td} & V_{ts} & V_{tb} \end{pmatrix} \tag{2.14}$$

In general, the n-dimensional unitary matrix has $n^2/2$ free parameters, $n(n-1)/2$ parameters for the rotational angles and $n(n+1)/2$ for phase factors. Cabbibo matrix has one rotational angle parameter, i.e. $\theta_{\rm C}$, and no phase factor. The CKM-matrix has three rotational angles and one phase factor. The phase factor is the origin of the CP violation.

To see why the phase factor may become the origin of the CP violation, let us consider the two amplitude of the diagrams in Figure 2.1.

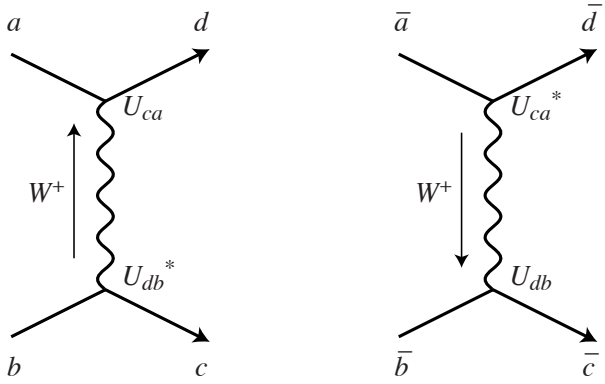

Figure 2.1: The left diagram shows $ab \to cd$ process. The right diagram is a charge conjugation of the left one. (It implies the parity transformation by itself.)

The right diagram is the process of anti-particles. It includes explicitly the charge conjugation, and implicitly the parity transformation. Because the weak interaction only couples between left-handed particles or the right-handed anti-particles.
The amplitude $\mathcal{M}$ of the left diagram is

$$\begin{aligned} \mathcal{M} &\sim J^{\mu}_{ca} J^{\dagger}_{\mu\, bd} \\ &\sim \left[\overline{u_c}\gamma^{\mu}\left(1-\gamma^5\right) U_{ca} u_a\right] \left[\overline{u_b}\gamma_{\mu}\left(1-\gamma^5\right) U_{bd} u_d\right]^{\dagger} \\ &\sim U_{ca} U^*_{db} \left[\overline{u_c}\gamma^{\mu}\left(1-\gamma^5\right) u_a\right] \left[\overline{u_d}\gamma_{\mu}\left(1-\gamma^5\right) u_b\right], \end{aligned} \tag{2.15}$$

here

$$U^{\dagger}_{bd} = U^*_{db}. \tag{2.16}$$

The amplitude $\mathcal{M}'$ of the right diagram is

$$\begin{aligned} \mathcal{M}' &\sim J^{\mu\,\dagger}_{ca} J_{\mu\, bd} \\ &\sim U^*_{ca} U_{db} \left[\overline{u_a}\gamma^{\mu}\left(1-\gamma^5\right) u_c\right] \left[\overline{u_b}\gamma_{\mu}\left(1-\gamma^5\right) u_d\right]. \end{aligned} \tag{2.17}$$

Therefore,

$$\mathcal{M} = \mathcal{M}^{\dagger}. \tag{2.18}$$

Let us perform CP transformation to the left diagram and the calculate its amplitude $\mathcal{M}_{CP}$. If

$$\mathcal{M}_{CP} = \mathcal{M}^{\dagger} \tag{2.19}$$

is satisfied, the CP is invariant, otherwise it is violated. The result of the calculation is

$$\mathcal{M}_{CP} \sim U_{ca} U_{db}^{*} \left[\overline{u_a}\gamma^{\mu}\left(1-\gamma^{5}\right) u_c\right] \left[\overline{u_b}\gamma_{\mu}\left(1-\gamma^{5}\right) u_d\right]. \tag{2.20}$$

If the matrix elements for the quark mixing are the real numbers, $\mathcal{M}_{CP} = \mathcal{M}^{\dagger}$ is satisfied, otherwise, i.e. if they are the complex numbers, $\mathcal{M}_{CP} \neq \mathcal{M}^{\dagger}$ occurs. Since Cabbibo matrix does not have the phase factor, it never yields the CP violation, while CKM-matrix which has one complex phase may emerge the CP violation.

For the CKM-matrix is the unitary, the elements satisfies the equation:

$$V_{ub}^{*} V_{ud} + V_{cb}^{*} V_{cd} + V_{tb}^{*} V_{td} = 0. \tag{2.21}$$

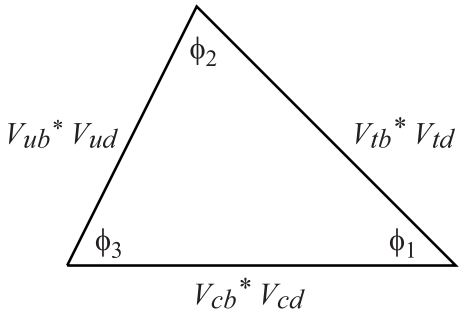

Figure 2.2: The unitary triangle of CKM-matrix. It is equivalent to eq. (2.21).

Figure 2.2 represents eq. (2.21) in the complex plane. The triangle is called as 'unitary triangle'. CKM-matrix is often represented by this triangle. Measuring the elements in CKM-matrix is equivalent to determine the three sides and the three angles of the unitary triangle.

2.4 CP Violation in B Decay

2.4.1 B^0-$\overline{B}^0$ Mixing

In this section, we describe the backbone theory to realize the measurement of the elements of CKM-matrix.

In the neutral B meson system, two B mesons $B^0$and $\overline{B}^0$mix with each other in the two types of the box diagrams shown in Figure 2.3.

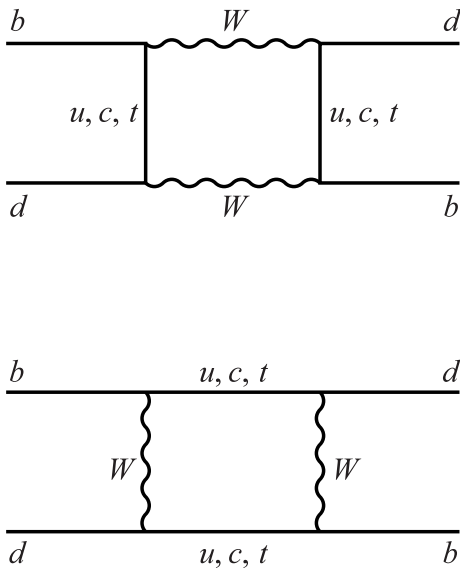

Figure 2.3: Two diagrams of the B^0-$\overline{B}^0$ mixing.

Both $B^0$and $\overline{B}^0$are the flavor eigenstates, but they are not the eigenstate of the mass.
Let us see that the mass eigenstates can be represented as the linear combination of $\left|B^0\right\rangle$ and $\left|\overline{B}^0\right\rangle$. We define the CP transformation as

$$CP\left|B^0\right\rangle = \eta_{CP}\left|\overline{B}^0\right\rangle, \tag{2.22}$$

where η_{CP} is the CP phase. CP phase can be chosen arbitrary, here we choose it as -1. The state of the B at the time of t can be written by the basis of $\left|B^0\right\rangle$ and $\left|\overline{B}^0\right\rangle$;

$$\left|B(t)\right\rangle = \alpha(t)\left|B^0\right\rangle + \beta(t)\left|\overline{B}^0\right\rangle \tag{2.23}$$

The time expansions of $\alpha(t)$ and $\beta(t)$ are written in the Shrödinger eq. (2.24)

$$\begin{aligned} \mathrm{i}\frac{\mathrm{d}}{\mathrm{d}t}\left|B(t)\right\rangle &= \mathcal{H}\left|B(t)\right\rangle \\ \mathrm{i}\frac{\mathrm{d}}{\mathrm{d}t}\begin{pmatrix}\alpha\\ \beta\end{pmatrix} &= \begin{bmatrix}\left\langle B^0\middle|\mathcal{H}\middle|B^0\right\rangle & \left\langle B^0\middle|\mathcal{H}\middle|\overline{B}^0\right\rangle \\ \left\langle \overline{B}^0\middle|\mathcal{H}\middle|B^0\right\rangle & \left\langle \overline{B}^0\middle|\mathcal{H}\middle|\overline{B}^0\right\rangle\end{bmatrix}\begin{pmatrix}\alpha\\ \beta\end{pmatrix} \end{aligned} \tag{2.24}$$

With rewriting $\mathcal{H}$ to $\mathcal{H} \equiv \mathcal{M} - (\mathrm{i}/2)\,\Gamma$, the matrix elements of the Hamiltonians $\mathcal{H}$ are defined as:

$$\begin{array}{ll} \left\langle B^0 \middle| \mathcal{H} \middle| B^0 \right\rangle \equiv \mathcal{M}_{11} - (\mathrm{i}/2)\,\Gamma_{11} & \left\langle B^0 \middle| \mathcal{H} \middle| \overline{B}^0 \right\rangle \equiv \mathcal{M}_{12} - (\mathrm{i}/2)\,\Gamma_{12} \\ \left\langle \overline{B}^0 \middle| \mathcal{H} \middle| B^0 \right\rangle \equiv \mathcal{M}_{21} - (\mathrm{i}/2)\,\Gamma_{21} & \left\langle \overline{B}^0 \middle| \mathcal{H} \middle| \overline{B}^0 \right\rangle \equiv \mathcal{M}_{22} - (\mathrm{i}/2)\,\Gamma_{22} \end{array} \tag{2.25}$$

For $\mathcal{H}$ is an Hermite matrix ($\mathcal{H} = \overline{\mathcal{H}^t}$),

$$\left\langle \overline{B}^0 \middle| \mathcal{H} \middle| B^0 \right\rangle = \mathcal{M}_{12}^* - (\mathrm{i}/2)\,\Gamma_{12}^*. \tag{2.26}$$

From the CPT conservation hypothesis,

$$\left\langle B^0 \middle| \mathcal{H} \middle| B^0 \right\rangle = \left\langle \overline{B}^0 \middle| \mathcal{H} \middle| \overline{B}^0 \right\rangle \equiv \mathcal{M}_0 - (\mathrm{i}/2)\,\Gamma_0. \tag{2.27}$$

The eigenvalues of $\mathcal{H}$ are given by $\mathcal{M}$ and Γ:

$$\lambda_\pm = \mathcal{M}_0 - (\mathrm{i}/2)\,\Gamma_0 \pm \sqrt{[\mathcal{M}_{12} - (\mathrm{i}/2)\,\Gamma_{12}][\mathcal{M}_{12}^* - (\mathrm{i}/2)\,\Gamma_{12}^*]}, \tag{2.28}$$

while their eigenstates are;

$$|B_\pm\rangle = \frac{1}{\sqrt{|p|^2 + |q|^2}} \left(p \left| B^0 \right\rangle \pm q \left| \overline{B}^0 \right\rangle \right), \tag{2.29}$$

where the correlation between p and q is

$$\frac{q}{p} = \frac{\sqrt{[\mathcal{M}_{12} - (\mathrm{i}/2)\,\Gamma_{12}][\mathcal{M}_{12}^* - (\mathrm{i}/2)\,\Gamma_{12}^*]}}{\mathcal{M}_{12} - (\mathrm{i}/2)\,\Gamma_{12}}. \tag{2.30}$$

Two eigenstates, $|B_+\rangle$ and $|B_-\rangle$ correspond to the eigenstates of the mass and the lifetime:

$$|B_+(t)\rangle = \mathrm{e}^{-\mathrm{i}\lambda_+} |B_+(0)\rangle = \mathrm{e}^{-\mathrm{i}\left[\mathrm{Re}\,(\lambda_+)\,t - \frac{1}{2}(-2\,\mathrm{Im}\,(\lambda_+))\right] t} |B_+(0)\rangle \tag{2.31}$$

$$|B_-(t)\rangle = \mathrm{e}^{-\mathrm{i}\lambda_-} |B_-(0)\rangle = \mathrm{e}^{-\mathrm{i}\left[\mathrm{Re}\,(\lambda_-)\,t - \frac{1}{2}(-2\,\mathrm{Im}\,(\lambda_-))\right] t} |B_-(0)\rangle \tag{2.32}$$

In equations (2.31) and (2.32), $\mathrm{Re}\,(\lambda_+)$ and $\mathrm{Re}\,(\lambda_-)$ are the mass of the two eigenstates. In the following discussion the heavier eigenstates are labeled as $|B_H\rangle$ instead of $|B_+\rangle$ and the lighter eigenstates are labeled as $|B_L\rangle$ instead of $|B_-\rangle$.

Let us write the eigenstates of the lifetime with the linear combination of the CP eigenstates. With the definition of the phase of η_{CP} made in eq. (2.22), the CP even state and CP odd state can be written as follows:

$$|B_e\rangle = \frac{1}{\sqrt{2}} \left(\left| B^0 \right\rangle - \left| \overline{B}^0 \right\rangle \right) \tag{2.33}$$

$$|B_o\rangle = \frac{1}{\sqrt{2}} \left(\left| B^0 \right\rangle + \left| \overline{B}^0 \right\rangle \right) \tag{2.34}$$

With these equations, two eigenstates of the lifetime are represented as

$$|B_H\rangle = \frac{1}{\sqrt{2(|p|^2+|q|^2)}}\left[(p-q)\,|B_e\rangle + (p+q)\,|B_o\rangle\right] \tag{2.35}$$

$$|B_L\rangle = \frac{1}{\sqrt{2(|p|^2+|q|^2)}}\left[(p+q)\,|B_e\rangle + (p-q)\,|B_o\rangle\right]. \tag{2.36}$$

Therefore, when $p = \pm q$ is satisfied, the lifetime eigenstates correspond to those of the CP transformation.

Next, let us see the time expansion of B mesons while their mixing. Here we assume that the B meson whose flavor at $t = 0$ is B^0. The initial state is

$$\left|B^0\right\rangle = \frac{\sqrt{|p|^2+|q|^2}}{2p}\left(|B_H\rangle + |B_L\rangle\right). \tag{2.37}$$

At the time t, the linear combination of $|B_H\rangle$ and $|B_L\rangle$ for $\left|B^0(t)\right\rangle$ becomes with equations (2.31) and (2.32):

$$\begin{aligned}\left|B^0(t)\right\rangle &= \frac{\sqrt{|p|^2+|q|^2}}{2p}\left(\mathrm{e}^{-\mathrm{i}\lambda_+ t}\,|B_H\rangle + \mathrm{e}^{-\mathrm{i}\lambda_- t}\,|B_L\rangle\right) \\ &= \frac{\mathrm{e}^{-\mathrm{i}\lambda_+ t}}{2}\left[g_+(t)\left|B^0\right\rangle + \frac{q}{p}g_-(t)\left|\overline{B}^0\right\rangle\right],\end{aligned} \tag{2.38}$$

where $g_\pm(t)$ is the function of t with parameters of the mass difference and lifetime difference between λ_+ and λ_-. If we define the mass difference as $\Delta\mathcal{M}$ and the lifetime difference as $\Delta\Gamma$, we obtain

$$\begin{aligned}\Delta\mathcal{M} &= \mathrm{Re}\,(\lambda_+ - \lambda_-) \\ &= 2\,\mathrm{Re}\left(\sqrt{[\mathcal{M}_{12} - (\mathrm{i}/2)\,\Gamma_{12}][\mathcal{M}^*_{12} - (\mathrm{i}/2)\,\Gamma^*_{12}]}\right)\end{aligned} \tag{2.39}$$

$$\begin{aligned}\Delta\Gamma &= -2\,\mathrm{Im}\,(\lambda_+ - \lambda_-) \\ &= -4\,\mathrm{Im}\left(\sqrt{[\mathcal{M}_{12} - (\mathrm{i}/2)\,\Gamma_{12}][\mathcal{M}^*_{12} - (\mathrm{i}/2)\,\Gamma^*_{12}]}\right) \\ &= \frac{4}{\Delta\mathcal{M}}\,\mathrm{Re}\,(\mathcal{M}_{12}\Gamma^*_{12}).\end{aligned} \tag{2.40}$$

With equations (2.39) and (2.40), $g_\pm(t)$ is written as follows:

$$g_\pm(t) \equiv 1 \pm \mathrm{e}^{\mathrm{i}[\Delta\mathcal{M} - (\mathrm{i}/2)\,\Delta\Gamma]t}. \tag{2.41}$$

2.4.2 Measurement of ϕ_1 – Decay Mode of $J/\psi\,K^0_S$

To measure ϕ_1 value, the decay mode of $b \to c\bar{c}s$ is used. The major CP eigenstate of this decay mode is $f_{CP} \equiv J/\psi\,K^0_S$ because this mode is free from the background. As for the physics analysis, J/ψ is reconstructed from two

leptons ($e^+ e^-$ or $\mu^+ \mu^-$) and K^0_S is reconstructed from two charged pions. This mode is called 'gold plated mode' or GPM. The branching fractions from B_{CP} to the GPM are listed in Table 2.1.

Table 2.1: The branching fractions from B_{CP} to the gold plated mode.

decay mode	branching fraction
$B_{CP} \to J/\psi\, K^0_S$	4.5×10^{-4}
$J/\psi \to \ell^+ \ell^-$	0.12
$K^0_S \to \pi^+ \pi^-$	0.68
Total	3.7×10^{-5}

In this section, the physics background for the measurement on ϕ_1 in CKM-matrix is described.

The decay probability of the $B^0 \to f_{CP}$ and $\overline{B}^0 \to f_{CP}$ (where f_{CP} is the final state of the CP eigenstate) at the time of t can be calculated with using eq. (2.40) as follows:

$$\Gamma(t; B^0 \to f_{CP}) = \frac{\mathrm{e}^{-(\Gamma_0 + \Delta\Gamma/2)t}}{4} \left| g_+(t) \left\langle f_{CP} \middle| B^0 \right\rangle + \frac{q}{p} g_-(t) \left\langle f_{CP} \middle| \overline{B}^0 \right\rangle \right|^2 \tag{2.42}$$

$$\Gamma(t; \overline{B}^0 \to f_{CP}) = \frac{\mathrm{e}^{-(\Gamma_0 + \Delta\Gamma/2)t}}{4} \left| \frac{q}{p} g_-(t) \left\langle f_{CP} \middle| B^0 \right\rangle + g_+(t) \left\langle f_{CP} \middle| \overline{B}^0 \right\rangle \right|^2 . \tag{2.43}$$

The CP eigenvalue of $\left| J/\psi\, K^0_S \right\rangle$ is -1. As we have already seen, K^0_S is not the real CP eigenstate, but we can neglect the CP violation effect because the violation is small in the K meson system.
There exist two Feynman diagrams for $B_{CP} \to J/\psi\, K^0_S$. The one is a 'tree diagram' (Figure 2.4).

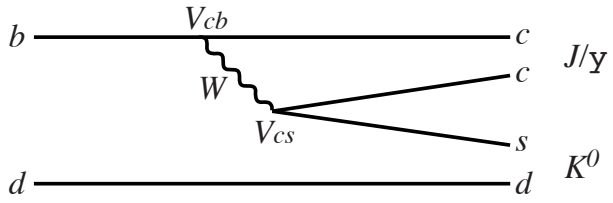

Figure 2.4: The tree diagram of $b \to c\bar{c}s$. In the gold plated mode, the contribution from the tree diagram is dominant.

From this diagram, the matrix element of $\langle J/\psi\, K^0 | B^0 \rangle$ is obtained:

$$\langle J/\psi\, K_S^0 \, | B^0 \rangle = V_{cb}^* V_{cs} A_t. \tag{2.44}$$

A factor which is not included to CKM-matrix is given by A_t.
Another diagram is called a "penguin diagram" (Figure 2.5).

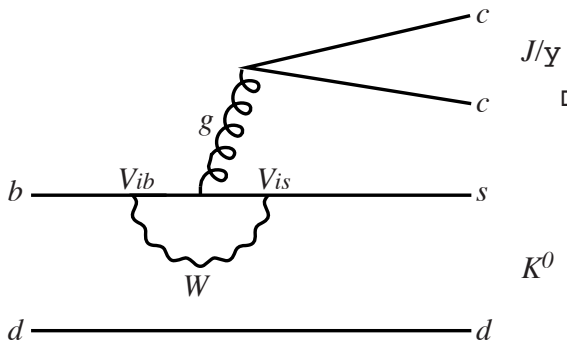

Figure 2.5: The penguin diagram of $b \to c\bar{c}s$. The contribution of the penguin diagram to the gold plated mode is negligible in comparison with the tree diagram.

We can neglect the contribution from this diagram. The penguin diagram has a factor $V_{ib}^* V_{is}$ for $i = u, c, t$. But $|V_{ub}^* V_{us}|$ is quite smaller than $|V_{cb}^* V_{cs}|$ and $|V_{tb}^* V_{ts}|$, $|V_{ub}^* V_{us}|$ can be ignored. And with the relation $\sum_{i=u,c,t} V_{ib}^* V_{is} = 0$ given by the triangle correlation eq. (2.21), we obtain

$$|V_{cb}^* V_{cs}| \simeq |V_{tb}^* V_{ts}|. \tag{2.45}$$

Therefore, the penguin diagram do not contribute to the measurement on the CP violation because of its small amplitude.
The matrix element of $\langle J/\psi\, K_S^0 | B_{CP} \rangle$ is extracted from the $\langle J/\psi\, K^0 | B_{CP} \rangle$ whose final state has the mixture of K^0 and $\overline{K}^0$. The amplitudes of the CP eigenstate are given like these:

$$\langle J/\psi\, K_S^0 \, | B^0 \rangle = \langle K_S^0 \, | K^0 \rangle \langle J/\psi\, K^0 \, | B^0 \rangle = \frac{p_K^*}{\sqrt{|p_K|^2 + |q_K|^2}} V_{cb}^* V_{cs} A_t \tag{2.46}$$

$$\left\langle J/\psi\, K_S^0 \, \middle| \overline{B}^0 \right\rangle = \frac{q_K^*}{\sqrt{|p_K|^2 + |q_K|^2}} V_{cb}^* V_{cs} A_t. \tag{2.47}$$

With the approximation of neglecting the CP violation,

$$\frac{q_K}{p_K} = \frac{V_{cd}V_{cs}^*}{V_{cd}^*V_{cs}} \tag{2.48}$$

is obtained. Here, $|V_{cd}^*V_{cs}| \gg |V_{td}^*V_{ts}|$ is used.
As for the B meson system, from eq. (2.30)

$$\frac{q}{p} = \frac{V_{td}V_{tb}^*}{V_{td}^*V_{tb}} \tag{2.49}$$

is derived by neglecting $\Gamma_{12}/\mathcal{M}_{12}$.
Finally, we obtain the calculation of eq. (2.43) as follows:

$$\Gamma(t; B^0 \to J/\psi\, K_S^0) \propto \mathrm{e}^{-|t|}\,(1 - \sin 2\phi_1 \sin \Delta\mathcal{M}t) \tag{2.50}$$

$$\Gamma(t; \overline{B}^0 \to J/\psi\, K_S^0) \propto \mathrm{e}^{-|t|}\,(1 + \sin 2\phi_1 \sin \Delta\mathcal{M}t)\,, \tag{2.51}$$

Or as the probability style,

$$P(t; B^0 \to J/\psi\, K_S^0) = \frac{1}{2}\mathrm{e}^{-|t|}\,(1 - \sin 2\phi_1 \sin \Delta\mathcal{M}t) \tag{2.52}$$

$$P(t; \overline{B}^0 \to J/\psi\, K_S^0) = \frac{1}{2}\mathrm{e}^{-|t|}\,(1 + \sin 2\phi_1 \sin \Delta\mathcal{M}t)\,, \tag{2.53}$$

are obtained.

2.5 Measurement of $\sin 2\phi_1$ in BELLE

Let us see how $\sin 2\phi_1$ is measured in the BELLE experiment.

2.5.1 $\sin 2\phi_1$ Measurement

First, $\Upsilon(4S)$, which is the resonance state of the $b\overline{b}$, is created from the collision of e^+ and e^-. The mass of $\Upsilon(4S)$ is $10.573\mathrm{GeV}/c^2$. $\Upsilon(4S)$ decays in very short time $< 10^{-21}$s into B^+B^- or $B^0\overline{B}^0$ in the same probabilities for each mode. Now we look into the mode of $\Upsilon(4S) \to B^0\overline{B}^0$.
We call a B meson which decays into $J/\psi\, K_S^0$ as B_{CP} and we call the associated B mesons of B_{CP} as B_{tag}. In the BELLE experiment, we must use following equations replacing t into Δt:

$$P(\Delta t; B^0 \to J/\psi\, K_S^0) = \frac{1}{2}\mathrm{e}^{-|\Delta t|}\,(1 - \sin 2\phi_1 \sin \Delta\mathcal{M}\Delta t) \tag{2.54}$$

$$P(t\Delta; \overline{B}^0 \to J/\psi\, K_S^0) = \frac{1}{2}\mathrm{e}^{-|\Delta t|}\,(1 + \sin 2\phi_1 \sin \Delta\mathcal{M}\Delta t)\,, \tag{2.55}$$

instead of eq. (2.52) and (2.53), where Δt is defined as

$$\Delta t \equiv t_{B_{CP}} - t_{B_{\rm tag}}. \tag{2.56}$$

Here, $t_{B_{CP}}$ and $t_{B_{\rm tag}}$ are the decay times of B_{CP} and $B_{\rm tag}$, respectively. Eq. (2.52) and (2.53) can be applicable only if at the time $t = 0$, the exact flavor of B is determined. Since B^0 and $\overline{B}^0$ mixes with each other, we can not say the flavor of each of them. The replacement leads that at the time $t = t_{B_{\rm tag}}$ we can determine the flavor of the partner meson B_{CP}. Let us see why the flavor of B_{CP} can be determined at the time $t = t_{B_{\rm tag}}$.
The spin of $\Upsilon(4S)$ is $+1$ because it is generated from the virtual photon. B^0 and $\overline{B}^0$ are the bosons of spin 0. Let us consider that if two B mesons from one $\Upsilon(4S)$ were B^0 at the same time, what would happen. For B^0's are the spin 0 particles, to conserve the angular momentum, the orbital angular momentum between two B^0 must be 1. Therefore the wave function for two B^0's becomes asymmetric, however it it not allowed as the state for two boson. The same logic is also applicable to the case of $\overline{B}^0$. Therefore, while mixing, they can not take neither two B^0 state nor two $\overline{B}^0$ state. In other word, when at a certain moment B is B^0, its partner B is $\overline{B}^0$, and vise versa.
Although we can not know the flavor of B_{CP} from its final state because the final state is the common decay mode for both B^0 and $\overline{B}^0$, we can know it from its partner $B_{\rm tag}$'s flavor, if $B_{\rm tag}$ does not decay into the CP eigenstate. Thus, from the flavor of $B_{\rm tag}$, we can know the flavor of B_{CP} at the moment $B_{\rm tag}$, which has a specified flavor, decays.

As described, in he BELLE experiment, the measurement of Δt is essential.
If the velocities of two B mesons are obtained, Δt can be calculated in this formula;

$$\Delta t = \frac{\Delta \ell_{B_{CP}}}{v_{B_{CP}}} - \frac{\Delta \ell_{B_{\rm tag}}}{v_{B_{\rm tag}}}, \tag{2.57}$$

where $\Delta \ell_{B_{CP}}$ and $\Delta \ell_{B_{\rm tag}}$ are the flight length of each B meson. Here, let us boost the $\Upsilon(4S)$ with a large boost factor for the z direction which corresponds to the beam axis. In the center of mass frame of the $\Upsilon(4S)$, two B mesons which are the decay yields of the $\Upsilon(4S)$, goes back to back. On the other hand, in the laboratory frame, two B mesons are boosted for the z direction with a boost factor that makes the transverse momentum of two B mesons negligible. Therefore, with the boost effect, we can approximately obtain the equations;

$$v_{B_{CP}z} \simeq v_{B_{\rm tag}z} \tag{2.58}$$

$$v_{B_{CP}T} \simeq v_{B_{\rm tag}T} \simeq 0. \tag{2.59}$$

And it follows that

$$\Delta \ell_{B_{CP}} \simeq \Delta z_{B_{CP}} \tag{2.60}$$

$$\Delta \ell_{B_{\rm tag}} \simeq \Delta z_{B_{\rm tag}}. \tag{2.61}$$

Then, eq. (2.57) can be written as

$$\Delta t \simeq \frac{\Delta z_{B_{CP}} - \Delta z_{B_{\rm tag}}}{v_{B_{CP}}} \tag{2.62}$$

$$\equiv \frac{\Delta z}{v_{B^0}}. \tag{2.63}$$

Here, Δz is the signed distance projected onto the z axis between the decay points of B_{CP} and $B_{\rm tag}$. In the BELLE experiment, measuring Δz is essential. And as we have already see, to obtain $\sin 2\phi_1$ is equivalent to obtain the distance of the decay vertecies of two B mesons projected onto z axis.

2.5.2 Flavor Tagging

While we should obtain Δz, we must also determine which equation, (2.52) or (2.53) should be applied for each event based on the flavor of B_{CP}. As described in the previous paragraph, the determination of the flavor of B_{CP} is equivalent to determine that of $B_{\rm tag}$. The procedure to determine the flavor of B_{CP} is called 'flavor tagging'.
The decay mode which is used well in the flavor tagging is

$$b \to c\,\ell^-\,\overline{\nu_\ell}. \tag{2.64}$$

There are several method to tag the flavor, and the better ones are still being researched. Generally ℓ^- of high momentum is the best signature of the the flavor of B_{CP}. Since ℓ^- directly comes from b quark, it has a high momentum. The second method is to search a high momentum K's that decays in

$$c \to s\,\ell^+\,\nu_\ell. \tag{2.65}$$

Wrong tagging of the B_{CP} flavor causes the smaller value of reconstructed $\sin 2\phi_1$. In case that wrong tag probability w exists, eq. (2.52) must be modified to

$$\begin{aligned} &P_{\rm measured}(t; B^0 \to J/\psi\, K_S^0) \\ &\quad = (1-w)\cdot\frac{1}{2}e^{-|\tau|}(1-\sin 2\phi_1 \sin x_d\tau) + w\cdot\frac{1}{2}e^{-|\tau|}(1+\sin 2\phi_1 \sin x_d\tau) \\ &\quad = \frac{1}{2}e^{-|\tau|}\left[1+(1-2w)\cdot\sin 2\phi_1 \sin x_d\tau\right]. \end{aligned} \tag{2.66}$$

The measured $\sin 2\phi_1$ becomes $(1-2w)\sin 2\phi_1$.
While the flavor tagging efficiency should be large, the wrong tag probability must be kept small. The parameter to see the optimization of these two paradoxical requirements is effective tag efficiency, defined by

$$\varepsilon_{\rm eff} = \epsilon(1-2w)^2. \tag{2.67}$$

In this equation, ϵ is the tag efficiency. Table 2.2 is the list of the current efficiency of the flavor tagging in the BELLE.

Table 2.2: The current status of the flavor tagging.

Tagging Method	Efficiency [%]	Wrong Prob. [%]	ε_{eff} [%]
Lepton Tag	12	4	10
Kaon Tag	34	13	18
Total	41	11	25

2.5.3 Measurement of Δz

To measure Δz, we must obtain two decay positions of B_{CP} and B_{tag}.
In the gold plated mode, the decay point of B_{CP} is substituted by the decay point of J/ψ since J/ψ has very short flight length less than $10^{-11}\mu$m. More than 10% of J/ψ decays into to two leptons ($e^+\,e^-$ or $\mu^+\,\mu^-$). Roughly speaking, the decay position is obtained by the vertex reconstruction from two leptons.
The measurement of the decay position of B_{tag} can not be simple. Since the tag side B yields charm meson which has the difficulty to reconstruct because of its various decay modes. Then, as the first approach, the high momentum lepton, which comes from B_{tag} is used to obtain the decay position of B_{tag}. The z position which gives the shortest distance from the track helix of the lepton and the z axis which is assumed as the beam axis. However, the beam axis is spread in the y direction, this method still should be optimized.

In addition to the advantage that the large boost factor for the z direction makes the problem of the Δt measurement easier.

Chapter 3

BELLE Experiment

3.1 Introduction

The BELLE experiment is optimized for the precise measurement of Δz. The accelerator is an asymmetric energy collider to give a boost factor to $\Upsilon(4S)$. As for the detectors, we have vertex detector with the good resolution to obtain the precise Δz values which is the essential role of the BELLE itself. The role for the flavor tagging is given to most detectors in the BELLE, especially to the K-π separation detector. In the procedure of the flavor tagging, we use K mesons which give the good information about the flavor of B_{CP} while π gives no information in spite that they exist too many. We use the threshold type detector for the purpose of the K-π separation.

In the BELLE experiment, we use the coordinate system shown in Figure 3.1.

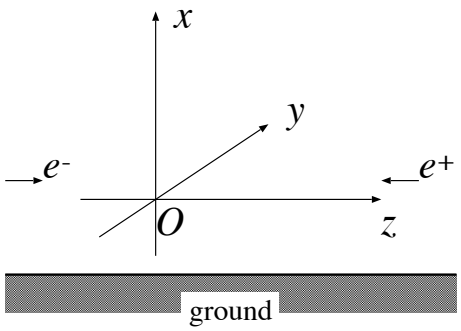

Figure 3.1: The coordinate system in the BELLE experiment.

The magnetic field is applied for the direction of $+z$.

3.2 Accelerator

Figure 3.2 is the accelerator for the BELLE experiment (KEKB).

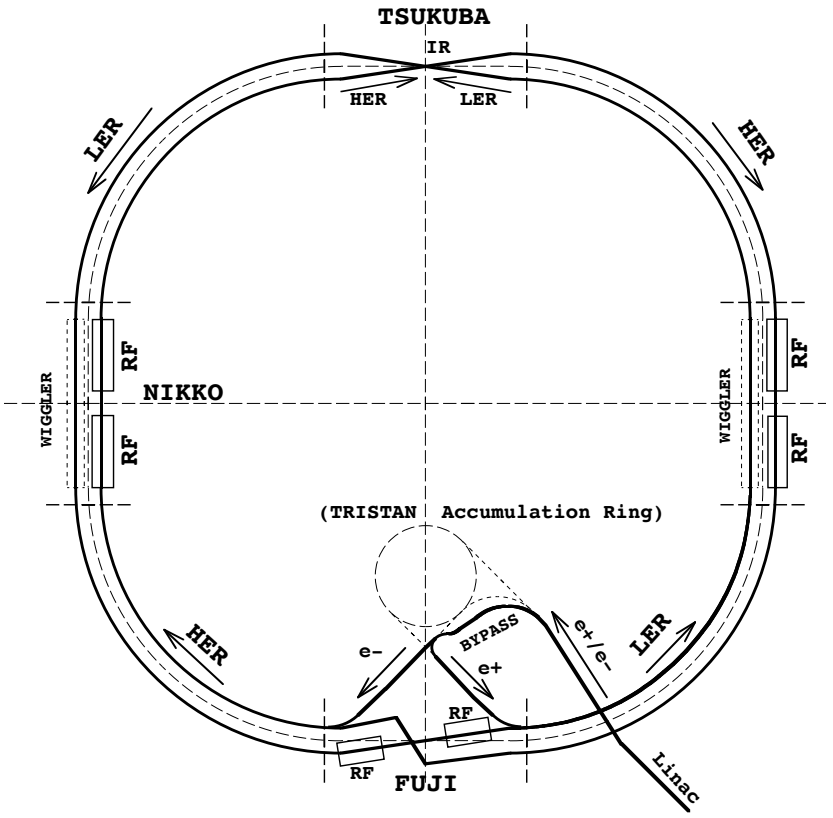

Figure 3.2: The BELLE accelerator

The accelerator is the $e^+\,e^-$ collider of asymmetric energy, with 8.0GeV electrons and 3.5GeV positrons. With the asymmetric energy, $\Upsilon(4S)$ is given the finite momentum in the laboratory frame which corresponds to $\beta\gamma = 0.425$. The total length of the accelerator is 3km. The maximum luminosity is $10^{34}\mathrm{cm}^{-2}\mathrm{s}^{-1}$. For the cross section of $e^+\,e^- \to \Upsilon(4S)$ is 1.2nb, the luminosity corresponds to the yield of 1.0×10^6 $\Upsilon(4S)$ in a day, and we have 38 gold plated events from these $\Upsilon(4S)$.

3.3 BELLE Detectors

BELLE is equipped with the detectors which are optimized for B physics study. Figure 3.3 is the global view of the BELLE detectors.

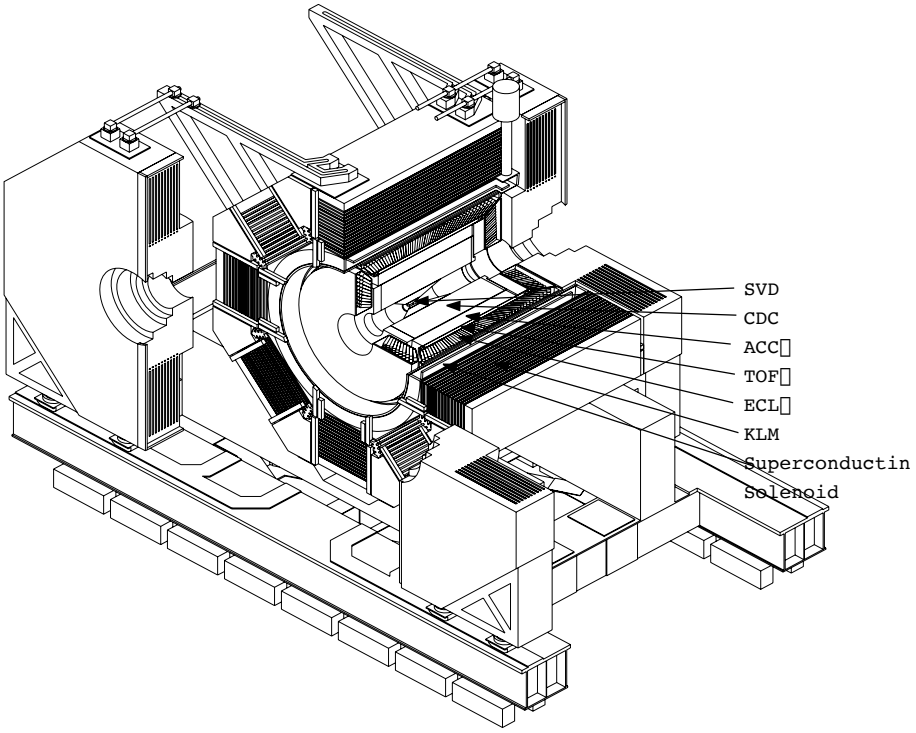

Figure 3.3: The overview of the BELLE detectors. From the inner, there exist SVD, CDC, ACC, TOF and ECL. The outermost detector is KLM which exist out of the magnetic field.

Silicon Vertex Detector (SVD)

The SVD is the vertex detector with precise vertex resolution. For the BELLE experiments requires the good resolution for the decay point reconstruction of B mesons, the precision of the vertexing is really essential.
The SVD consists of three layers of silicon ladders, with covering the polar angle from 21° to 140°.
The angle coverage corresponds to the acceptance of 87%. The vertex position is obtained by the interpolation of the reconstructed track by the CDC, while the precision of Δz is expected to be better than $80\mu m$.

Central Drift Chamber (CDC)

The primary role of the CDC is the detection of a charged particle track and the reconstruction of its momentum. The magnetic field of 1.5T is applied to the detector region. There exist ununiformity in the magnetic field, which can be negligible for the fast tracking study. The polar angle coverage of the CDC is from 17° to 150°. The outermost wires exist at the radius $r = 874.0$mm and in z from $z = -702.2$mm to $z = 1502.2$mm. This corresponds to the angle coverage from 29° to 129°. The radius $r = 874.0$mm corresponds to the transverse momentum $P_T = 197\text{MeV}/c$.

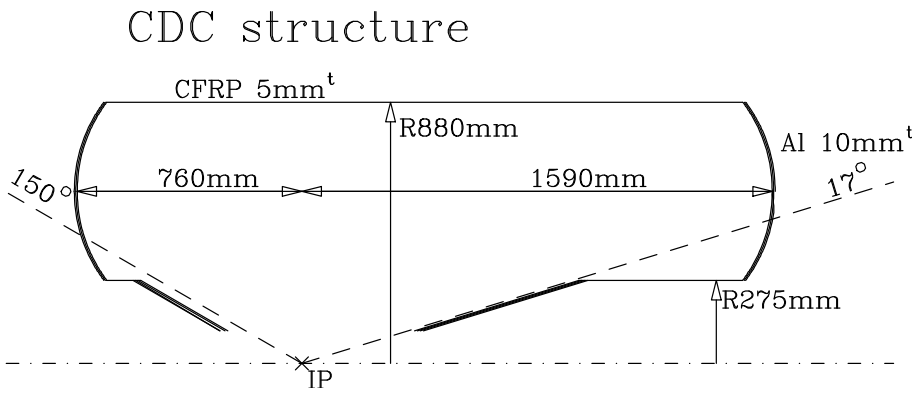

Figure 3.4: The side view of the CDC.

The CDC consists of 8,400 sense wires 1,500 cathode readout planes. There exist 50 wire layers in the CDC, 32 for the axial wire layers, and 18 for the stereo wire layers. The axial wires are put parallel to the beam axis and the stereo wires have a small angle less than 100mrad with respect to the beam axis. The cathode strips are provided to measure the z-coordinates at the innermost radii. They are aligned to orthogonal to the axial wire layers. We have 3 cathode layers in each of which 8 cathode channels exist.
The resolutions of the CDC are $\sigma_{r\phi} = 130\mu$m and $\sigma_z = 200 \sim 1400\mu$m. We estimate the precision of CDC track reconstruction is $\sigma_P/P \simeq 0.006$.
Another role is the particle identification with $\mathrm{d}E/\mathrm{d}x$. The CDC has the responsibility of the particle identification for the tracks whose momentum is $P \leq 600\text{MeV}/c$. The error of $\sigma_{\mathrm{d}E/\mathrm{d}x} = 6\%$.

The CDC is filled two types of gases. The one is the helium and the other is the ethane. They, which have low Z, are chosen to reduce the multiple scattering.

Aerogel Čerenkov Counter (ACC)

The ACC, which is one of the featuring detectors in the BELLE experiment, is for separation of kaons and pions for the momentum region in $1.2 < P < 3.5\mathrm{GeV}/c$. The aerogel of the ACC is the SiO_2 whose reflective index is $n \simeq 1.015$.
In general, when an particle with the velocity β goes into a matter with the reflective index of n, the Čerenkov light is emitted if eq. (3.1) is satisfied.

$$n > \frac{1}{\beta} = \sqrt{1 + \left(\frac{m}{P}\right)^2}. \tag{3.1}$$

With the track momentum reconstructed by the CDC, the particle can be identified whether it emitted a light or not.
The ACC covers the polar angle from 33.3° to 127.9°.

Time of Flight Counter (TOF)

The TOF, which is made from a plastic syntilation counter, is also for the particle identification. It has the responsibility to identify the charged particles whose momentum is less than $1.2\mathrm{GeV}/c$. The relation between the measured flight time T and the particle mass is as follows:

$$T = \frac{L}{c}\sqrt{1 + \left(\frac{m}{P}\right)^2}, \tag{3.2}$$

where L is the flight length. The polar angle coverage of the TOF is from 33.7° to 120.8°.
In addition, the TOF has one another scintillation counter. It is called Thin Scintillation Counter (TSC). The TSCs are used for the trigger signal generation.

Electromagnetic Calorimeter (ECL)

The main role of the ECL is the detection of photons and electrons with catching the electrons generated by the electromagnetic shower. Since it is expected that many π^0 come from the decay of B, reconstruction of γ and π^0 is necessary for the study. The ECL is used not only the previous purpose but also the measurement of the luminosity by the Bhabha scattering which yields high energetic electrons. Thus the ECL covers the energy range widely from 20MeV to 8GeV. The ECL is made of the CsI crystals.

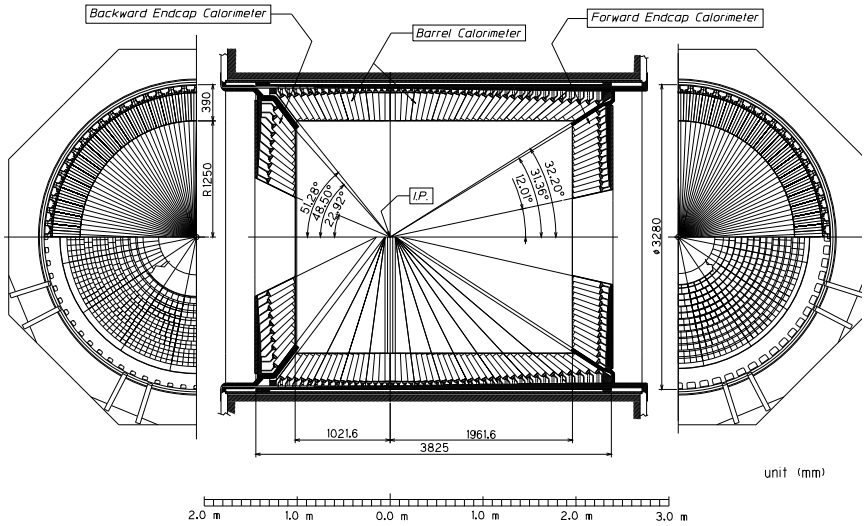

Figure 3.5: The overall configuration of ECL.

K_L and Muon Catcher (KLM)

The KLM is the outermost detector for the separation of K_L^0 and μ, which exist out of the magnetic field. Because the decay of

$$B_{CP} \to J/\psi K_L^0 \tag{3.3}$$

has the same branching fraction of the goals plated mode and the final state of the decay mode (3.3) is also the CP eigenstate, the effort for the detection of K_L^0 is necessary.
The KLM consists of the octagonal barrel detector and forward and rear endcap detectors. The detector consists of the piled up iron plates and detector plates (RPC). In the barrel region there exist 15 layers for iron plates and 14 layers for RPC, while in the endcap region there are 14 layers for both iron plates and RPC.
The iron plates are the energy absorber for the K_L^0. Because K_L^0 loses its energy by the strong interaction with the iron plates, while μ which does not feel the strong force penetrates the all iron plates, the K_L^0 can be separated from muons by catching the anihialated particles in the KLM.
The KLM can not measure the momentum of K_L^0. It measures the polar angle of K_L^0.

3.4 Data Flow Scheme at BELLE

Figure 3.6 shows the global data flow scheme in the BELLE experiment.

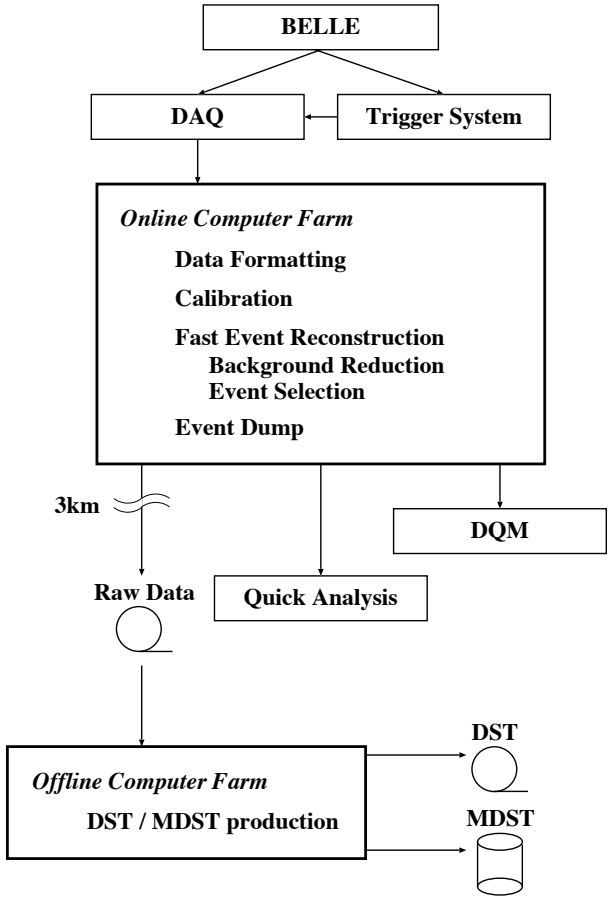

Figure 3.6: The global data flow scheme in the BELLE experiment.

The trigger signals from the CDC, TSC, ECL and EFC are sent to the global decision logic (GDL) to be examined whether the data should be taken or not [6]. The trigger decision logic is programmable so that it can be optimized based on real data. The trigger rates for both physics processes and backgrounds are estimated to be $\sim$ 100Hz. This results in total trigger rate of about 200Hz.

The BELLE data acquisition system (DAQ) is segmented into ~ 10 subsystems, they run in parallel. The data from each subsystem is combined into a single event record by an event builder, which converts the 'detector-by-detector' parallel streams to an 'event-by-event' data river. The event builder sends the data to an online computer farm, where another level of event processing is done. The DAQ system is designed to be tolerant against the trigger rate up to 500Hz which corresponds to four times of the expected background rate.

The event data is processed on the online computer farm. The online computer farm consists of six VME crates, each equipped with 20 Motorola RISC chips (MC88100). The total CPU power is about 3000MIPS. The online farm performs event-by-event parallel processing in which each event data is processed by one CPU.
Figure 3.7 shows an architecture of the online computer farm.

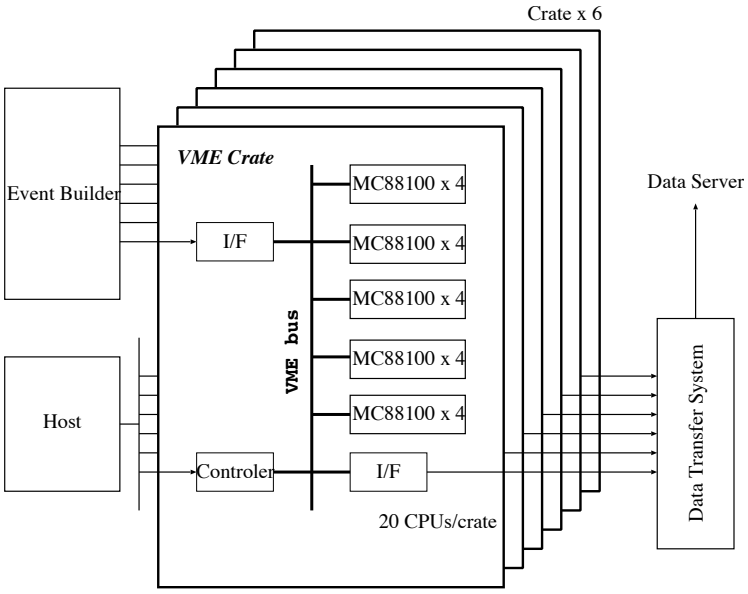

Figure 3.7: The architecture of the online computer farm.

On the online computer farm the following processings are performed:

- Data formatting
  Raw data from the DAQ system is converted into the BELLE standard data format.
- Calibration
  Pedestals are subtracted from raw data and electronics gains are corrected.

More complicated calibration will be performed on the offline computer farm.

- Event reconstruction
  Charged tracks are reconstructed to monitor the detector performance, to reject background events and to classify the events. It is important to detect any detector problem by monitoring the performance in real time. The background events are discarded while keeping as many signal events as possible, to save the storage space and the processing time of the offline computer farm. Events are classified into hadronic and leptonic events. A large fraction of leptonic events are discarded since limited amount of those events are necessary for calibration.

- Event dump
  The processed data are then sent to the computer center which is located 3km away from the experimental hall via optical fiber cable and they are dumped onto the tape.

The raw data written onto the tape are cooked into the data summary tape (DST) by the offline computer farm. The offline computer farm consist of 7 boxes of SPARC UltraEnterprise in each of which 28 SPARC chips exist. The total CPU power of the offline computer farm is about 50,000MIPS.

I developed an online track reconstruction program fast enough to be tolerant against the maximum trigger rate of 500Hz.

Chapter 4

Online Event Reconstruction

4.1 Introduction

Track reconstruction is an essential part of the online event reconstruction. The number of the tracks in each event gives good information about the event. For example, the leptonic events typically have two tracks, hadronic events have three or more. With the track momentum information , we can check the momentum balance in the r-ϕ plane or z direction. Low momentum tracks are not reconstructed since they do not change the event characteristics so much. It significantly reduce the time required for event reconstruction.

Since the event reconstruction must be performed at the maximum DAQ rate of 500Hz, some track reconstruction algorithms which may be common for the offline analysis are not acceptable for the online purpose.
To achieve the fast performance, we use the data from the trigger system instead of the detectors, which is well summarized for the online use.

The track reconstruction consists of track finding in r-ϕ plane, momentum reconstruction in r-ϕ plane and momentum reconstruction in the z direction. First, tracks are found in the r-ϕ plane with the memory lookup method which is one of the fastest algorithms for the pattern recognition. The track finder uses the trigger signals from the CDC r-ϕ trigger. Then the momentum in the r-ϕ plane (P_T) is calculated using the hit wire positions in the found track. Finally, the r-ϕ track is associated with the information of the CDC r-z trigger to obtain the P_z value.

4.2 Track Finding in r-ϕ Plane

The track finding in the r-ϕ plane is performed with the memory lookup method, which is one of the fastest methods in the pattern recognition problem, if the number of the lookup patterns is the reasonable or the searching method is fast enough.

4.2.1 Data Input

Since we have 5,280 axial wires in the CDC, if we might use the wire hit pattern as the lookup table, the number of the pattern becomes enormous. This is not a realistic solution. Thus, we use the summarized hit information from the trigger system.
The CDC generates two types of the track trigger. an r-ϕ track trigger and an r-z track trigger.

The CDC consists of 32 axial wire layers, in which the wires are parallel to the beam axis, and stereo wires have a small angle (< 100mrad) respect to the beam axis. The 32 axial wire layers are grouped into six super-layers.
In each super-layer, the axial wires are grouped into some segments to generate 'grouped hit signals'. The wire groups are called track segment finders (TSFs). Figure 4.1 shows the six super-layers.

Table 4.1: Configuration of super-layers.

super-layer ID	number of axial wire layers	number of TSFs	radius (mm)
1	6	64	118.25
2	6	96	264.0
3	5	144	400.0
4	5	192	544.0
5	5	240	688.0
6	5	288	832.0

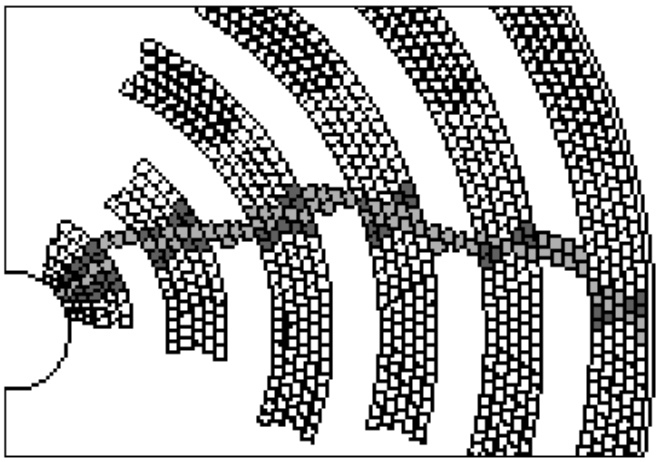

Figure 4.1: The overview of the CDC r-ϕ trigger. The light hatched points represent the fired wire cells and the heavy hatched are represents the fired TSFs.

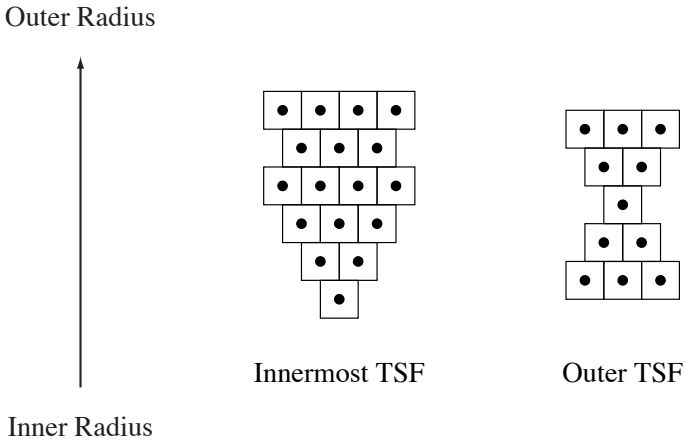

Figure 4.2: The shapes of the TSFs. The left shape is for the innermost super-layer and the right one is for the outer super-layers. The squares are the cell of the wires and the dots in the cell represent the wires.

In Figure 4.2, the shapes of the TSFs are shown.

The TSFs in the innermost super-layer consist of six wire layers and those in other super-layers consist of five wire layers, Figure 4.3 shows an overlapped regions of TSFs. Because of their special shapes, TSFs have overlapped regions with its neighbors. In other words, one wire cell belongs to two or more TSFs, except for the innermost wire cells in the innermost super-layer and the center wire cells in the outer super-layers.

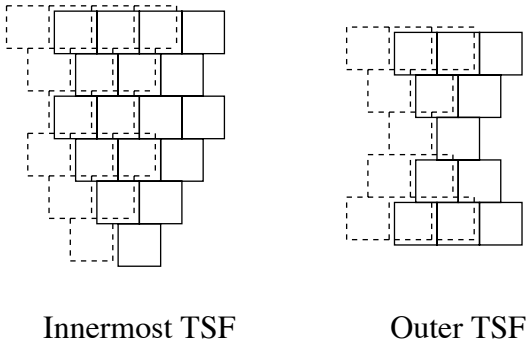

Figure 4.3: The overlapped regions of the TSFs. The next TSF is represented by the broken line. The TSFs are aligned to have the overlapped regions with their neighbors.

The TSF generates hit signals when its wire hit pattern matches the stored lookup patterns. Figure 4.4 shows some examples of the TSF hit patterns.

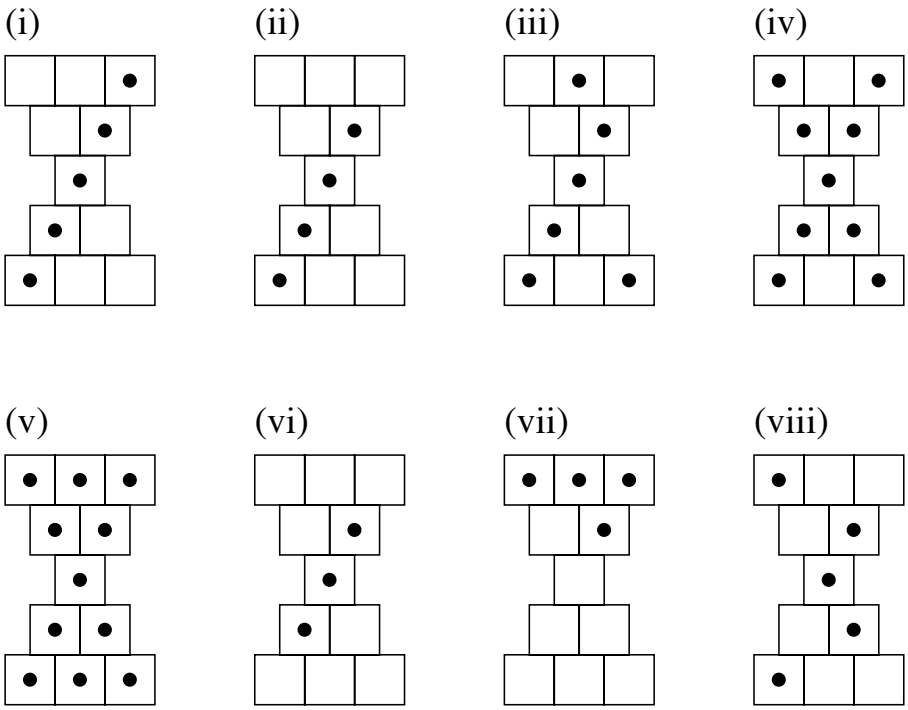

Figure 4.4: Eight examples of TSF hit patterns. The dots represent the hit wire cells. (i) $\sim$ (v) indicate valid patterns and (vi) $\sim$ (viii) indicate invalid patterns.

The valid lookup pattern is generated by a simulation study. Basically, the hit signal is generated when a track penetrates all wire layers (case (i)). Missing one wire cell hit is allowed (case (ii)). In addition to case (ii), any hit such as noise hit is allowed (case (iii)). Thus, the case that two tracks come into the one TSF (case (iv)) and that all wire cells are hit (case (v)) are also allowed. On the other hand, case (vi) is not allowed because it has two missing wire cell hits. In case (vii), the track might traverse the outermost wire layer, but it does not penetrate all wire layers of TSF. Therefore, it is not a valid pattern. Although all wire layers have the wire hit cells, case (viii) is not allowed, because a real track never generates such hit patterns.
The numbers of the lookup patterns for each super-layer is 2^{17} for the innermost super-layer and 2^{11} for other super-layers. The inefficiency of the CDC wire cell hit is expected to be less than 2%. The TSF efficiency is greater than 99.6%.

4.2.2 Definition of Data Pattern

We have 1024 TSFs, which is too many. We first find hit TSFs in the outermost super-layer. And only TSFs close to the line defined by the outermost hit TSF and the interaction point are considered to reduce the number of TSFs we have to manage.
When we define minimum transverse momentum ($P_{T\min}$), all the hits produced by tracks with $P_T \geq P_{T\min}$ should be in the hatched region shown in Figure 4.5. The two arcs with an arrow in Figure 4.5 represent positive and negative tracks with $P_{T\min}$

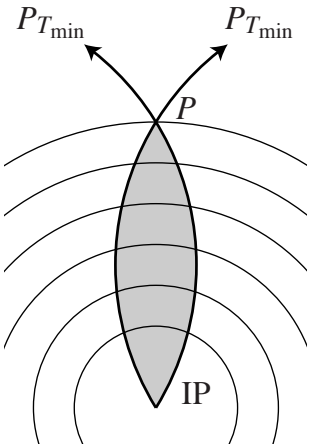

Figure 4.5: Arcs represent the tracks whose have the minimum transverse momentum $P_{T\min}$ in the reconstruction of P_T. The thin six arcs are the super-layers. The tracks which cross the point P must exist the hatched area when it has greater transverse momentum than $P_{T\min}$.

Only TSFs in the hatched are are used for the track finding. To reduce the number of TSFs (n) in the hatched area, $P_{T\min}$ must be raised. Figure 4.6 shows the relationship between the number of TSFs and $P_{T\min}$.

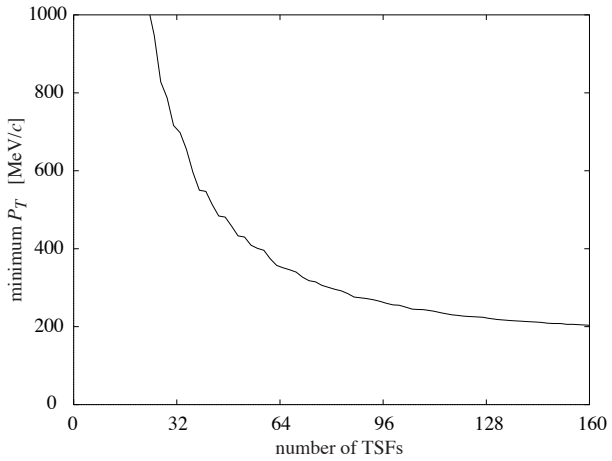

Figure 4.6: The minimum P_T which is representable by the n-width lookup pattern. The horizontal axis is number of bit-width n.

We choose $n = 64$ which correspond to $P_{T\min} \sim 350\text{MeV}/c$. When $n = 32$, $P_{T\min} \sim 600\text{MeV}/c$ which seems too large. When $n = 96$, $P_{T\min} \sim 250\text{MeV}/c$ which is not so different from that for $n = 64$. Table 4.2 lists the number of TSF in the hatched region in each super-layer when $n = 64$.

Table 4.2: The numbers of the checked TSFs.

super-layer	number of checked TSFs
5	11
4	13
3	15
2	13
1	11

TSF hit pattern in the hatched region is represented by a 64-bit word. To be exact, it is represented by two 32-bit words because the integer width of the online computer farm is 32 bits. Figure 4.7 shows an arrangement of the TSFs in the 64-bit word corresponding to an example shown in Figure 4.8.

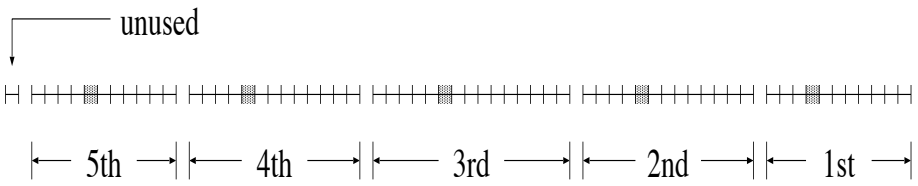

Figure 4.7: The data pattern corresponds to Figure 4.8.

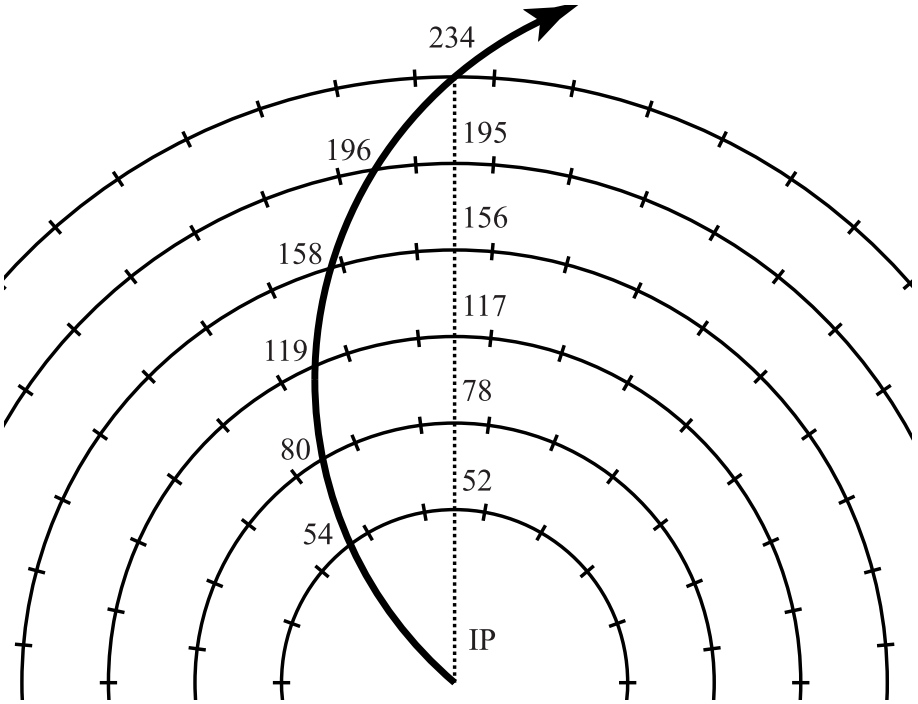

Figure 4.8: A track from the interaction point (IP) fires 234th TSFs.

The hatched bits, which are represented as 1 in the pattern, corresponds to the hit TSFs. In the fourth super-layer region, the 9th bit is hatched. For the 7th bit is the center bit in the fourth super-layer, it corresponds to the TSF id of 156, and 158th TSF is represented by the 9th bit.

4.2.3 Track Recognition

Tracks are recognized when data pattern matches valid data pattern (lookup pattern).

The data pattern is tested by taking the logical-AND with each of the lookup pattern. The data pattern must be tested against all of the lookup patterns since there may be more than one lookup patterns which matches the data pattern. Figure 4.9 and Figure 4.10 demonstrate a case in which the data pattern has two matched lookup patterns shown in Figure 4.11.

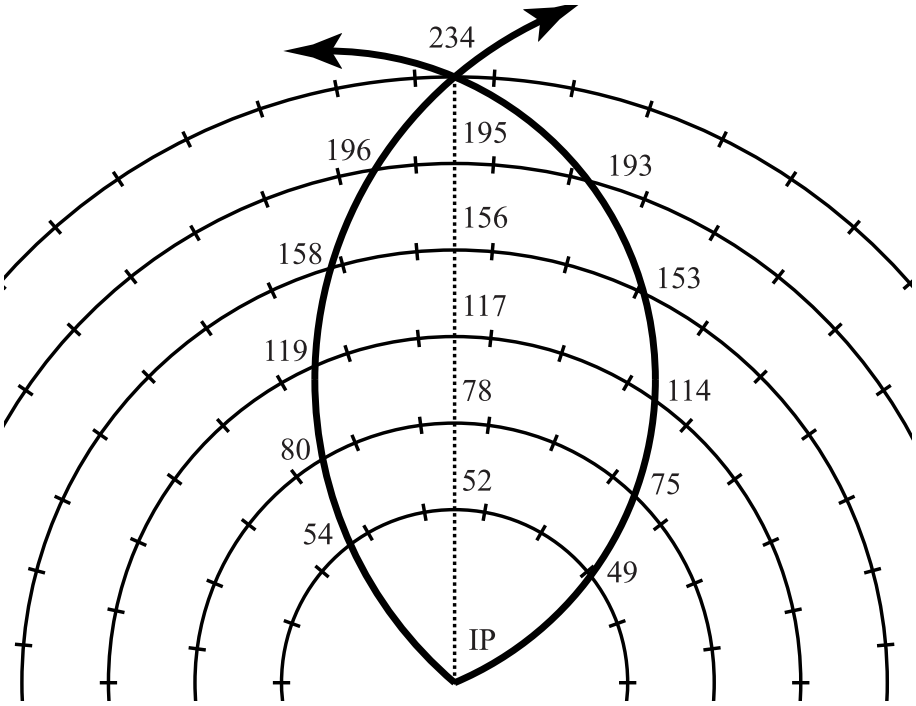

Figure 4.9: Two tracks from the IP fire the 234th TSF.

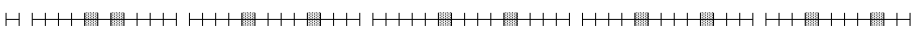

Figure 4.10: The data pattern corresponds to Figure 4.9.

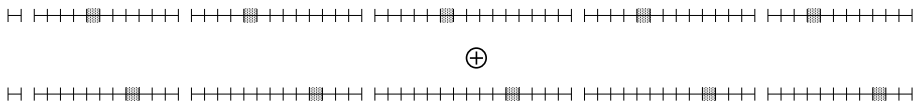

Figure 4.11: The data pattern shown in Figure 4.10 can be divided into two patterns. These two patterns can be found in the lookup table.

4.2.4 Creation of Lookup Tables

The lookup table is a collection of valid data patterns. The track figure in the r-ϕ plane is represented as a function of ϕ;

$$\phi(r) = \cos^{-1}\left(1 - \frac{R^2}{2\rho^2}\right) - \cos^{-1}\left(1 - \frac{r^2}{2\rho^2}\right), \tag{4.1}$$

where ρ is the radius of the track;

$$\rho[\mathrm{m}] = \frac{P_T[\mathrm{MeV}/c]}{B[\mathrm{T}] \times c[\mathrm{m/s}]} \times 10^6. \tag{4.2}$$

The P_T is varied from 200 MeV/c to 10GeV/c, which is near about beam energy, by 1MeV/c step. By this step, the pattern is bound to one corresponding momentum. Then the same patterns are united to be one. The gathered pattern is given the momentum rage which yields the pattern. Figure 4.12 shows the pattern coverage. One pattern covers the momentum range enclosed by two vertical lines.

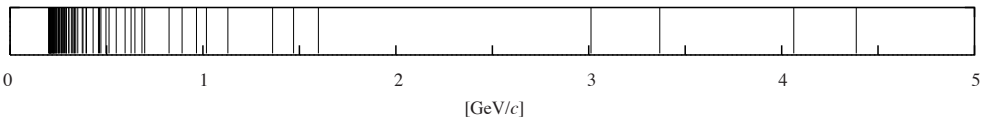

Figure 4.12: The pattern coverage of the range of P_T. One segment corresponds to the coverage of the P_T range of the lookup pattern.

Figure 4.8 shows the case that all five TSFs just beneath the 234th outermost TSF are aligned. However, they are not not always aligned. When we look at the 236th outermost TSF as an example, we can easily understand the inalignment of the inner TSFs. The alignment period of the TSF is the greatest common divider among the numbers of the TSFs in each super-layer. It is 18. Therefore, 18 sets of the lookup patterns are necessary. Figure 4.12 is the pattern set for the TSFs whose id number is the multiple of 18.

4.2.5 Modification of Lookup Patterns

However, there are many tracks which do not fire the TSF predicted by eq (4.1). In many case, these tracks fire the neighbor TSFs of the prediction. To salvage the fallen tracks from the track finding, the patterns are modified to allow the neighbor TSF hits. In the new pattern, allowed TSF width is changed from one to three in each super-layer.

4.2.6 Fake Track Rejection

Since one track often hit more than one TSFs in each super-layer, duplicated tracks are found from one track. When two patterns yields non-zero value by the calculation of logical-AND, they are merged into single track.

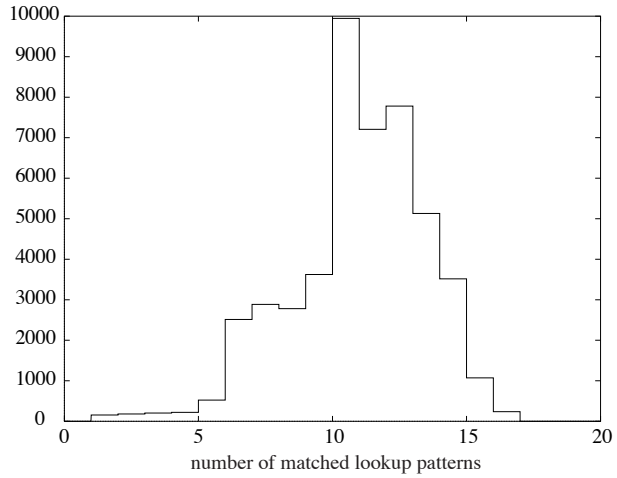

Figure 4.13: The number of matched lookup patterns for a single track. A data pattern generated by a single track can match about 10 lookup patterns.

Figure 4.13 shows the number of lookup patterns for a single track before and after the above duplicated track rejection.

4.2.7 Reconstruction Efficiency

Figure 4.14 is the track finding efficiency as a function of generated transverse momentum P_T.

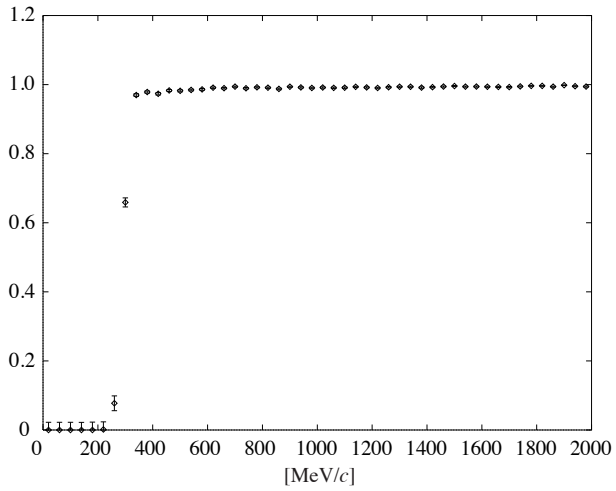

Figure 4.14: The track finding efficiency as a function of P_T. Almost all tracks whose transverse momentum is more than 500MeV/c are found.

To perform the test, single μ^+ is generated for each of 100,000 events within the CDC acceptance region. The transverse momentum of the generated track is varied from 0MeV/c to 2GeV/c. The track finding efficiency for the region $P_T > 500$MeV/c is almost 100% .

Figure 4.14 is the plot of the track finding efficiency against the polar angle.

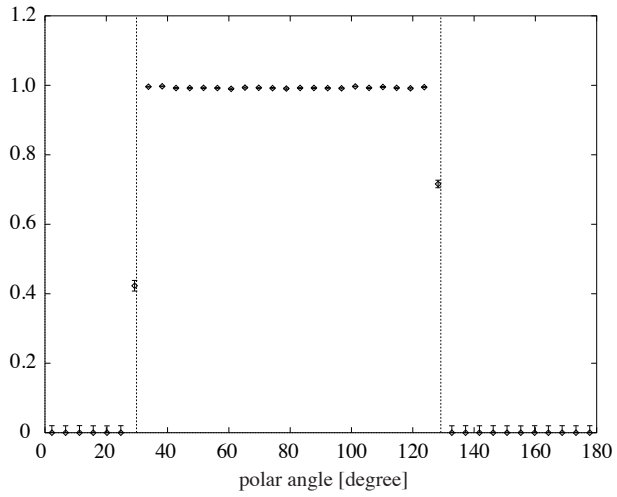

Figure 4.15: The track finding efficiency as a function of the polar angle of the generated track. Almost all tracks within the CDC angle coverage are found. The CDC covers from 29° to 129°. The angle coverage limits are shown by the broken line in Figure.

The track finder finds all tracks within the CDC angle coverage from 29° to 133°.

As described above, the track finder finds the only tracks which come from the interaction point. Figure 4.16 shows the reconstruction efficiency as a function of the generation vertex projected onto the r-ϕ plane.

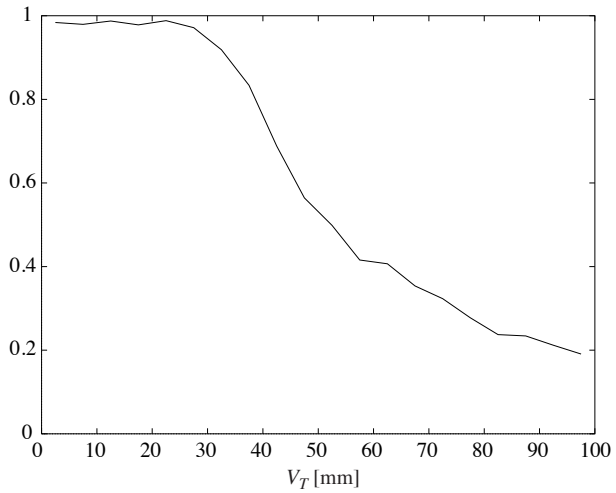

Figure 4.16: The track finding efficiency as a function of V_T. Here V_T is defined as the distance form the interaction point to the generation point of the tracks projected on the r-ϕ plane.

In this study, 20,000 2GeV/c μ^+ Monte Carlo tracks are generated within the CDC region. The track finder finds the tracks whose generation vertices exist 20mm away from the generation point.

Figure 4.17 shows an example of the reconstructed tracks for the $b\overline{b}$ events.

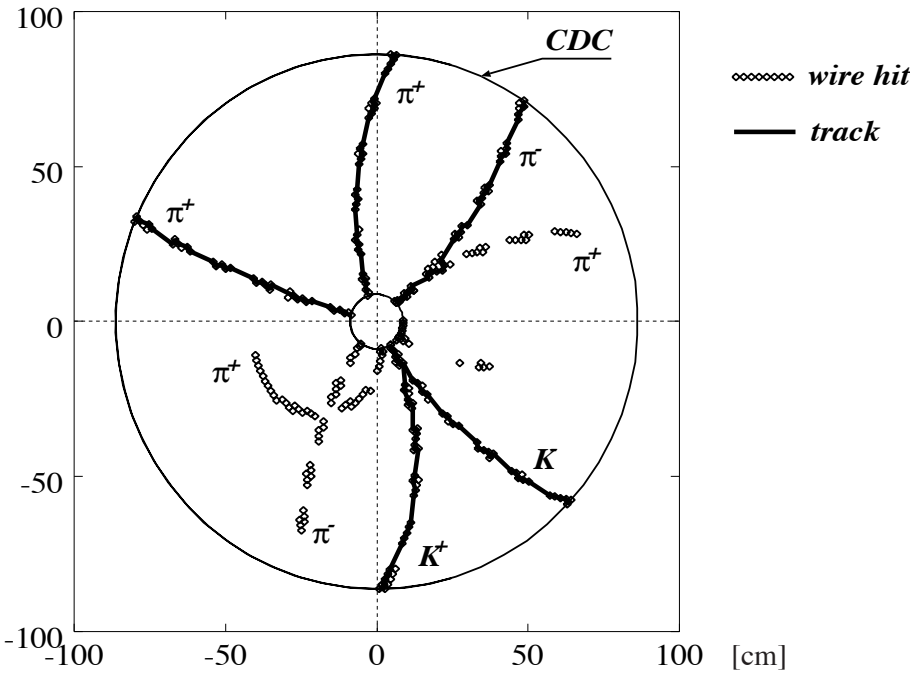

Figure 4.17: The performance example of the track finder for a $b\overline{b}$ event. Each square corresponds to the wire hit and the tick arcs are the reconstructed tracks.

In this example, 3 tracks are not reconstructed, since they do not reach the outermost super-layer.

4.3 Momentum Reconstruction in r-ϕ Plane

4.3.1 Reconstruction with Lookup Pattern

The P_T of the found track can be given by the central value of the possible P_T range of the matched lookup patterns. Figure 4.18 shows the $\Delta P_T/P_T$ distribution.

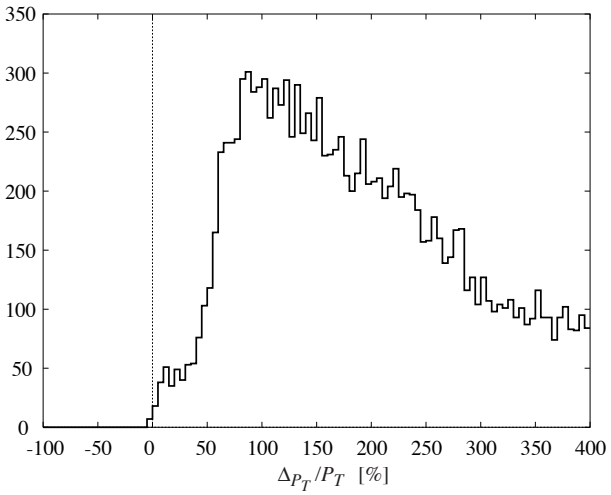

Figure 4.18: The momentum reconstruction with lookup pattern. The reconstructed P_T are much greater than the Monte Carlo values of P_T.

The resolution is pretty bad since a track usually match about 10 lookup patterns and momentum range is very large.
The track momentum is reconstructed by applying the circle fit to the hit wire positions in the associated TSFs to improve momentum resolution. The pitch of the wires is about 15mm.

4.3.2 Methods of Momentum Reconstruction

Two algorithms of the track fitting are compared in terms of the momentum resolution and the speed.
In the following sections, I use the notations of (x_c, y_c) for the center of the track, R for the radius of the track, $\{\boldsymbol{w}_i\} \equiv (x_i, y_i)$ for the position of the hit wires. Since the track finder finds only the tracks from the origin of x-y plane, the radius and the center of the track are related in the equation of

$$R^2 = x_c^2 + y_c^2 \tag{4.3}$$

Other new parameters are defined where they appears.
When (x_c, y_c) is obtained, the track momentum for the charged particle P_x and P_y are

$$P_x[\mathrm{GeV/c}] = -B[\mathrm{T}]\, c[\mathrm{m/s}]\, y_c[\mathrm{m}] \times 10^{-10} \tag{4.4}$$

$$P_y[\mathrm{GeV/c}] = B[\mathrm{T}]\, c[\mathrm{m/s}]\, x_c[\mathrm{m}] \times 10^{-10}, \tag{4.5}$$

where B is the magnetic field (1.5T) and c is the light velocity.

4.3.2.1 Conformal Plane Method

An arc which crosses the origin of the x-y plane is transformed to the segmented line in X-Y plane by eq. (4.6)

$$\begin{pmatrix} X \\ Y \end{pmatrix} \equiv \frac{2}{x^2+y^2} \begin{pmatrix} x \\ y \end{pmatrix}. \tag{4.6}$$

Reconstruction speed is expected to be fast since track parameters can be obtained by linear fit.
Figure 4.19 indicates the transformation.

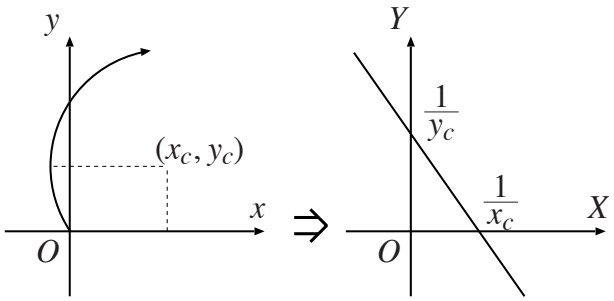

Figure 4.19: The conformal transformation. By the conformal transformation, an arc which crosses the origin of x-y plane is transformed to the segmented line in the conformal plane (X-Y plane).

This transformation is called a 'conformal transformation', and the transformed X-Y plane is called a 'conformal plane'. The center of the arc (x_c, y_c) correspond to $1/X_0$ and $1/Y_0$ as shown in Figure (4.19). The radius of the track R corresponds to the inverse of the distance from origin of X-Y plane to the line in the conformal plane.
The fitting error Δ_i should be given as the distance from the conformal point (X_i, Y_i) to the line $Y = a + bX$. Least square fit is too difficult with this definitions, thus X component of Δ_i is ignored. Then Δ_i becomes quite simple:

$$\Delta_i \equiv \frac{1}{\sigma_i}\{Y_i - (a + bX_i)\}. \tag{4.7}$$

The error of Δ_i (i.e. σ_i) is r_i^2 which is the distance from the beam axis to the wire position in the real r-ϕ plane.

$$\begin{aligned} \sigma &\simeq \delta_X \\ &\simeq \delta\left(\frac{2x}{x^2+y^2}\right) \\ &\propto \frac{1}{r^2}. \end{aligned} \tag{4.8}$$

The free parameters a and b are obtained as:

$$a = \frac{1}{\alpha}\left(\left[X_i^2\right]\left[Y_i\right] - \left[X_i\right]\left[X_iY_i\right]\right) \tag{4.9}$$

$$b = \frac{1}{\alpha}\left(\left[1\right]\left[X_iY_i\right] - \left[X_i\right]\left[X_iY_i\right]\right), \tag{4.10}$$

$$\tag{4.11}$$

where

$$\alpha = \left[1\right]\left[X_i^2\right] - \left[X_i\right]^2. \tag{4.12}$$

Here $[x]$ is the weighted mean of x_i, i.e.:

$$[x] \equiv \frac{1}{n}\sum_i^n \frac{x_i}{\sigma_i^2}. \tag{4.13}$$

Since the wire hit positions is given by its geometrical information, each values in the brackets in eq. (4.9), (4.10) and (4.12) are constants. Therefore, the pre-calculations of those values, such as X_i^2/σ_i^2, X_iY_i/σ_i^2, X_i/σ_i^2, Y_i/σ_i^2, and $1/\sigma_i^2$ can be made to reduce the fitting time.
Finally, (x_c, y_c) is obtained:

$$x_c = -\frac{a}{b} \tag{4.14}$$

$$y_c = a. \tag{4.15}$$

4.3.2.2 Linear Approximation Method [7]

Track parameters are obtained by a fit to a circle.

The reconstruction error can be given by

$$\Delta R_i = \sqrt{(x_i - x_c)^2 + (y_i - y_c)^2} - R. \tag{4.16}$$

Actually, this is a very poor definition of ΔR_i from the view point of the requirement for the fast performance. This definition is not the linear function of neither x_c nor y_c. Generally the minimization of non-linear function takes a lot of time, since the minimization requires some sort of the iteration.
Let us consider to define Δ_i expressed by the linear function of x_c and y_c.

With the constraint of eq. (4.3), the difference between the squares of the distance from a point (x, y) to the origin and to a circle is given by

$$\Delta(R^2) = (x - x_c)^2 + (y - y_c)^2. \tag{4.17}$$

The distance from the point to the circle is given approximately by

$$\Delta R \simeq \frac{\Delta(R^2)}{2R} = \frac{1}{2R}\left(x^2 + y^2\right) - \frac{x_c}{R}x - \frac{y_c}{R}y \tag{4.18}$$

Here we give special symbols to the coefficients in eq. (4.18)

$$\Delta R \simeq \kappa r + \alpha x + \beta y, \tag{4.19}$$

where

$$\kappa \equiv \frac{1}{2R} \tag{4.20}$$

$$\alpha \equiv -\frac{x_c}{R} \tag{4.21}$$

$$\beta \equiv -\frac{y_c}{R}. \tag{4.22}$$

The square sum is represented by these parameters as

$$\mathcal{S}(\alpha, \beta, \kappa) = \sum_i \frac{1}{\sigma_i^2} \left(\kappa r_i + \alpha x_i + \beta y_i\right)^2 \tag{4.23}$$

Thus we obtain the square sum $\mathcal{S}$ which is the linear combination of κ, α and β.
Two equations eq. (4.21) and eq. (4.22) are related as follows:

$$\alpha^2 + \beta^2 = 1. \tag{4.24}$$

Although it seems there exist three parameters, the number of the free parameters among them is two.
The minimization of eq. (4.23) under the constraint of eq. (4.24) is equivalent to solve

$$\frac{\partial}{\partial(\alpha, \beta, \kappa)} \left\{\mathcal{S} - \lambda\left(\alpha^2 + \beta^2 - 1\right)\right\} = 0 \tag{4.25}$$

with the good selection of λ.
In the matrix representation

$$\begin{pmatrix} \left[x_i^2\right] - \lambda & \left[x_i y_i\right] & \left[x_i r_i^2\right] \\ \left[x_i y_i\right] & \left[y_i^2\right] - \lambda & \left[y_i r_i^2\right] \\ \left[x_i r_i^2\right] & \left[y_i r_i^2\right] & \left[r_i^4\right] \end{pmatrix} \begin{pmatrix} \alpha \\ \beta \\ \kappa \end{pmatrix} = 0. \tag{4.26}$$

In terms of matrix, if non-trivial set of (α, β, κ) exists, the determinant of the matrix in eq. (4.26) must be 0. It follows that the rank of the matrix is not 3, which is consistent to the fact that the number of the free parameter is 2.
To make the determination zero, we need to choose the valid λ by solving the quadratic equation in eq. (4.26). Two roots are calculated by the formula:

$$\lambda_\pm = \frac{-b \pm \sqrt{b^2 - 4ac}}{2a}, \tag{4.27}$$

where

$$a \equiv \left[r_i^4\right]$$

$$b \equiv -\left[r_i^4\right]\left(\left[x_i^2\right] + \left[y_i^2\right]\right) + \left[x_i r_i^2\right]^2 + \left[y_i r_i^2\right]^2 \tag{4.28}$$

$$c \equiv \left[r_i^4\right]\left(\left[x_i^2\right]\left[y_i^2\right] - \left[x_i y_i\right]^2\right) + 2\left[x_i y_i\right]\left[x_i r_i^2\right]\left[y_i r_i^2\right] - \left[x_i r_i^2\right]^2\left[y_i^2\right] - \left[y_i r_i^2\right]^2\left[x_i^2\right].$$

The existence of two λ implies that there exist two minimals in $\mathcal{S}(\alpha, \beta, \kappa)$. Two patterns are shown by Figure 4.20.

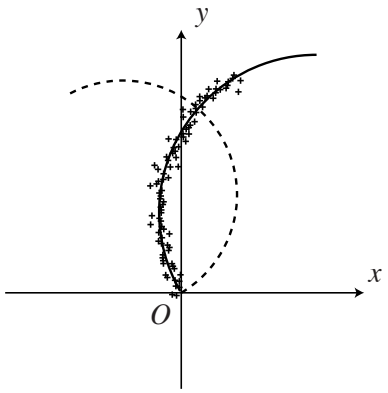

Figure 4.20: There exist two roots for the quadratic equation of λ (eq. (4.27)). The crosses represent the hit wire positions. The solid arc is a reconstructed 'real' track and the dashed arc is a 'fake' track.

The fitted track is always given by λ_- and the 'fake track' is given by λ_+. Once λ is obtained, substituting λ to eq. (4.26), two equations are obtained,

$$\begin{cases} p\alpha + q\kappa = 0 \\ s\beta + t\kappa = 0 \end{cases} \tag{4.29}$$

Finally, x_c and y_c is obtained by

$$x_c = \frac{\alpha}{2\kappa} = -\frac{q}{p} \tag{4.30}$$

$$y_c = \frac{\alpha}{2\kappa} = -\frac{t}{s}. \tag{4.31}$$

In this method, the pre-calculation of those values, such as r_i^4, $x_i r_i^2$, $y_i r_i^2$, x_i^2, $x_i y_i$, and y_i^2, can be made to speed up the calculation.

4.3.2.3 Comparison of The Fitting Method

Figure 4.21 shows the comparison of the P_T resolution between the conformal plane method and the linear approximation method.

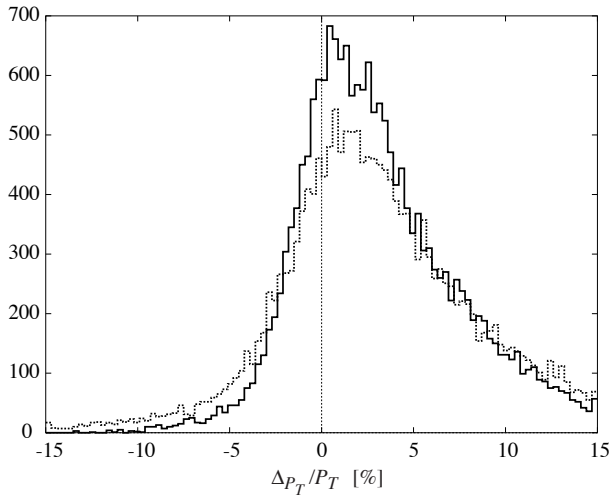

Figure 4.21: The error distribution of the reconstructed transverse momentum for the reconstructed tracks.

The dotted and solid histogram indicates the $\Delta P_T/P_T$ distribution for the conformal plane method and for the the linear approximation method, respectively. In this study, 20,000 μ^+ are generated within the CDC region. Their momenta are varied from 400MeV/c to 2GeV/c. The linear approximation method gives slightly better resolution. Asymmetry and the shift of the mean in the distribution can be seen. This is caused by inefficient track finder since the fit using all hits gives no asymmetry as shown in Figure 4.22.

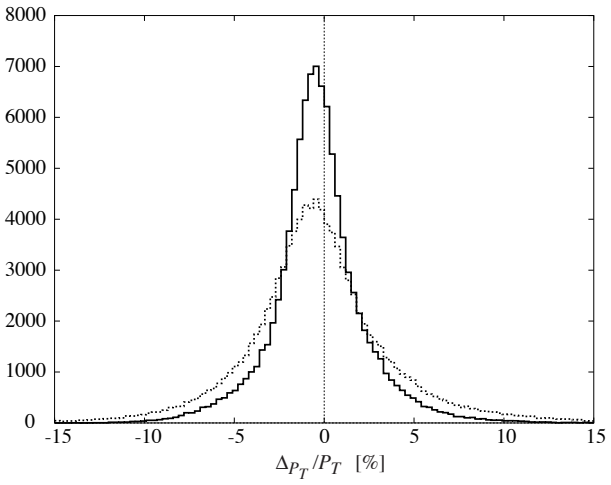

Figure 4.22: The error distribution of the reconstructed transverse momentum with the energy loss effect of the track. The shift to the negative direction can be seen. 100,000 μ^+ tracks are generated within the CDC acceptance with varying P_T from 400MeV/c to 2GeV/c^2.

Mean shift to negative value still remains. It is caused by the energy loss effect since the distribution does not show the shift if energy loss effect is turned off in the simulation as shown in Figure 4.23.

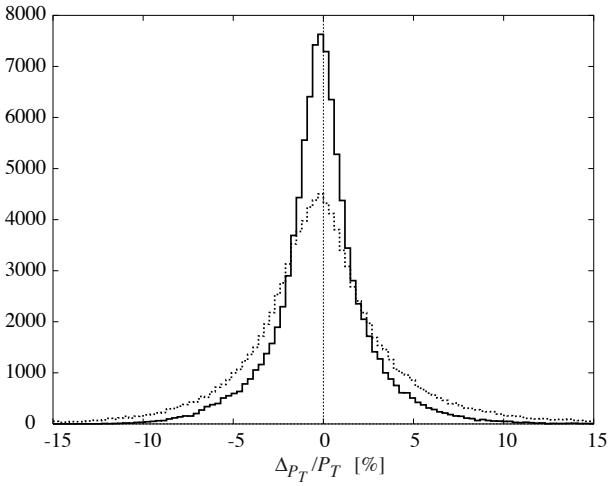

Figure 4.23: The error distribution of the reconstructed transverse momentum without the energy loss effect of the track.

In the following discussion, the 'Linear Approximation Method' is undertaken.

Figure 4.24 shows the reconstruction error of P_T as a function of generated P_T.

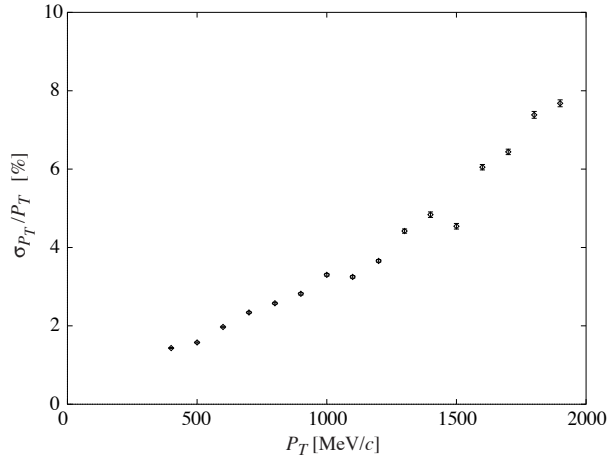

Figure 4.24: The reconstruction error of P_T defined by the standard distribution of $(P_{T\,\mathrm{rec.}} - P_{T\,\mathrm{gen.}})/P_{T\,\mathrm{gen.}}$ as a function of P_T.

The relation is measured to be

$$\sigma_{P_T}/P_T\ [\%] = 3.5 \times P_T[\mathrm{GeV}/c] \tag{4.32}$$

4.3.3 Charge Determination

The charge can be determined by the sign of

$$\begin{pmatrix} x_i \\ y_i \end{pmatrix} \times \begin{pmatrix} x_c \\ y_c \end{pmatrix}. \tag{4.33}$$

The track finder never finds the curl tracks such as which wrap their center position, the hit wire (or say the index i) can be chosen arbitrary. For the negative charged track, the signs of P_x and P_y are inverted.

4.4 Momentum Reconstruction in z Direction

After P_T is obtained for the r-ϕ track, z trigger [8] is associated to the track. θ information from the associated z trigger is used to obtain P_z value. $P_z = 0$ is given when no z trigger information can be associated.

4.4.1 z Trigger Association

We have two kinds of z trigger information, stereo z trigger information and cathode z trigger information. For the z trigger information, the polar angle is divided into 30 segments as shown in Figure 4.25 and the r-ϕ plane is divided into eight segments equally as shown in Figure 4.26. The z trigger gives θ and ϕ segments which track pass through. When the r-ϕ track is in the ϕ segment given by a z trigger, the r-ϕ track is associated with the z trigger. θ value of the track is defined as the center of the θ range given by the θ segment of the associated z trigger
The P_z value is calculated as $P_z = P_T/\tan\theta$.

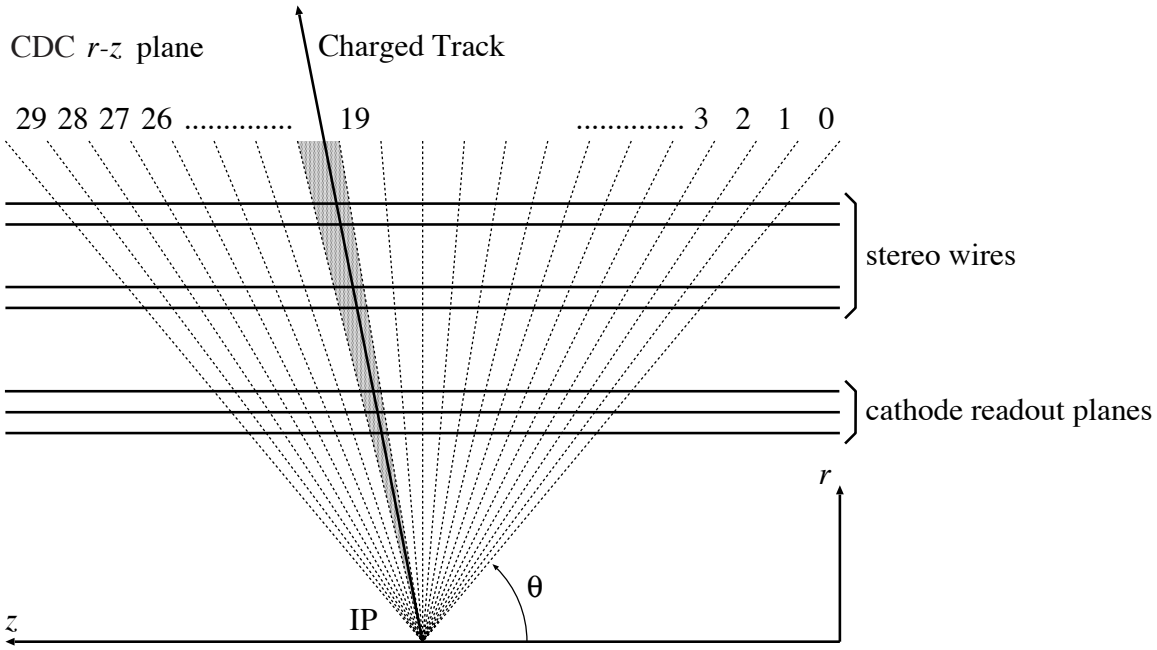

Figure 4.25: The side view of the CDC r-z trigger. The generated seven integers are called 'trigger tower'.

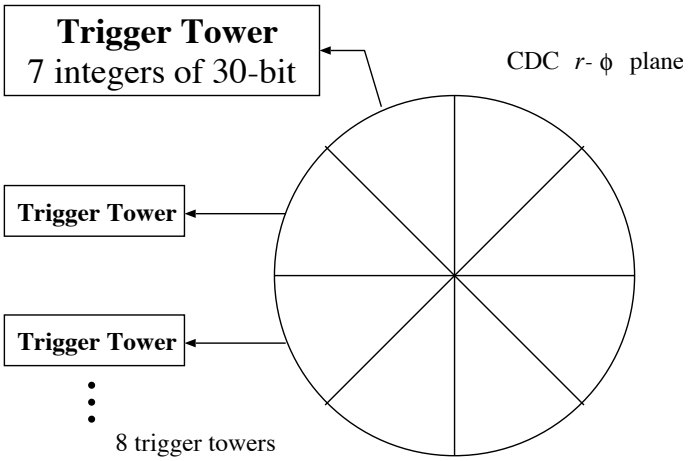

Figure 4.26: The trigger towers are generated for each of one eighth of the CDC r-ϕ plane.

4.4.2 Resolution Study

Resolutions are studied for the polar angles of 90°, 40° and 120°. All tracks are generated at the transverse momentum of 2.0GeV/c. The number of the generated tracks are 10,000. Figures 4.27 are comparisons of $\theta_{\mathrm{rec.}} - \theta_{\mathrm{gen.}}$ in the unit of degree between the cathode and stereo θ informations, respectively. The values of $\theta_{\mathrm{rec.}} - \theta_{\mathrm{gen.}}$ is quantized since $\theta_{\mathrm{gen.}}$ are exact values and $\theta_{\mathrm{rec.}}$ are quantized.

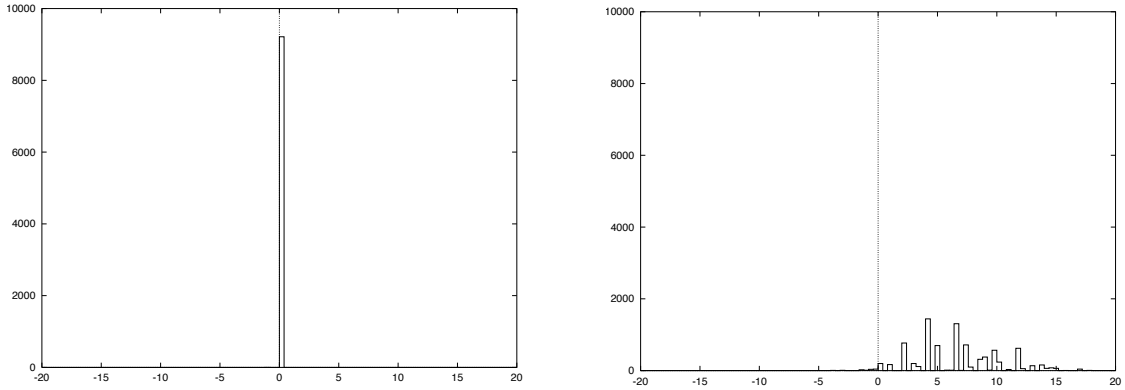

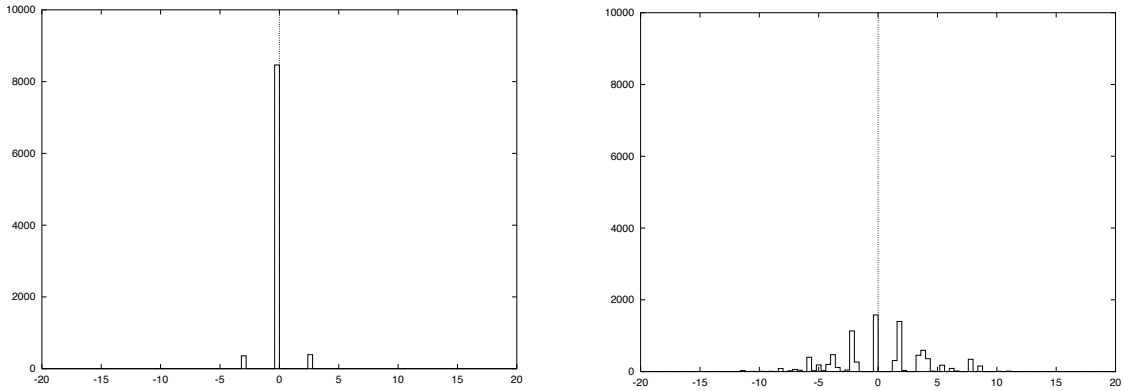

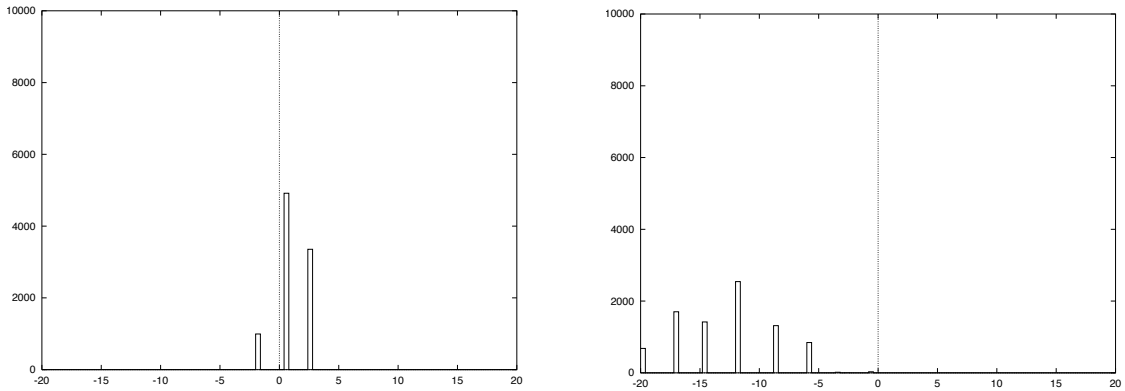

Figure 4.27: The comparison between the cathode read out planes and the axial wires for the use of the measuring device of polar angle of the track. The horizontal axis is $\theta_{\mathrm{rec.}} - \theta_{\mathrm{gen.}}$[degree] where θ is the polar angle of the track.

The cathode θ resolution is better than the stereo θ resolution. Mean value of the $\theta_{\mathrm{rec.}} - \theta_{\mathrm{gen.}}$ for stereo z trigger is shifted from 0 when polar angle is not 90°. Clearly the cathode θ information is better than the stereo θ information. Cathode θ information is used to calculate P_z when it is available, otherwise stereo θ information is used.

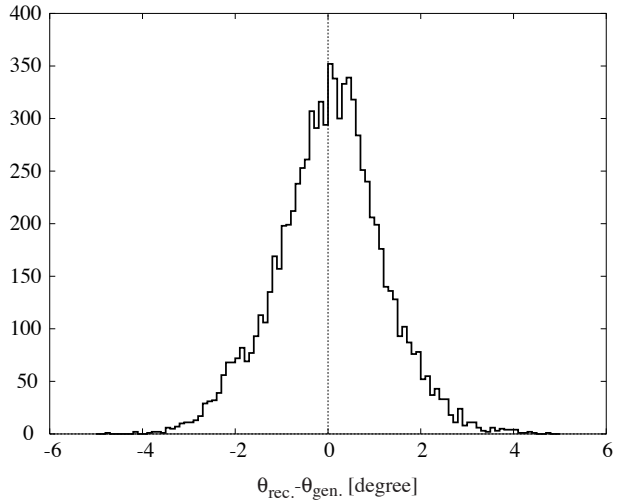

Figure 4.28: The error distribution of the reconstructed polar angle with the CDC r-z trigger signals generated on the CDC cathode readout planes.

The reconstruction error of cathode θ information is shown in Figure 4.28. Among 10,000 μ^+ tracks generated, 8,610 tracks are reconstructed. The distribution is not quantized because $\theta_{\mathrm{gen.}}$ is continuous.

Figure 4.29 shows the distribution of $(P_{z\,\mathrm{rec.}} - P_{z\,\mathrm{gen.}})/P_{z\,\mathrm{gen.}}$. In this study, 100,000 μ^+ tracks are generated within the CDC angle acceptance ($29° < \theta < 129°$) with varying its P_T from 0MeV/c to 2MeV/c.

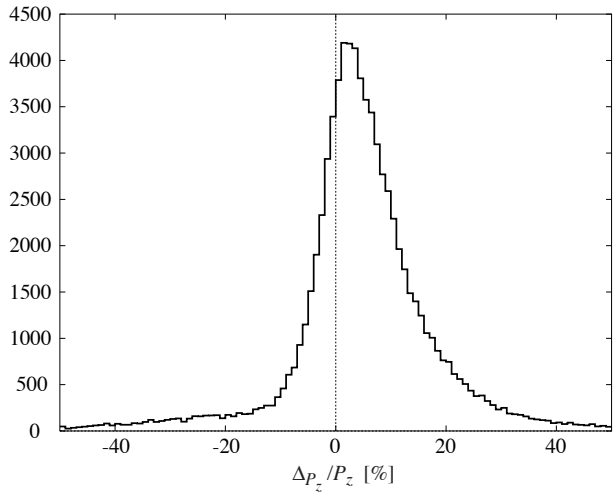

Figure 4.29: The error distribution of the reconstructed z directional momentum with the CDC r-z trigger signals.

The distribution indicates that the reconstructed P_z value tends to be larger then the generated value. This can be attributed to the fact that reconstructed P_T value tends to be larger than the generated value.

Chapter 5

Applications of Event Reconstruction

In this chapter, the performance study for the application of the event reconstruction is described. First, a track reconstruction efficiency for the $b\overline{b}$ event is shown. Then, the output of the physics monitor is shown, and with using the monitored values, the event classification is performed. Finally, the processing speed is mentioned.

5.1 Physics Monitor

With the reconstructed tracks, we can have the monitor values for the physics events.
The simulation studies have been made for each event type of $b\overline{b}$ events, continuum events ($q\overline{q}$), the Bhabha scattering, and $e^+ e^- \to \mu^+ \mu^-$ process,
Since the Bhabha events have large differential cross section in the forward region, events which does not satisfy trigger conditions are discarded to minimize the simulation time. In this study temporary trigger conditions are given as follows because the trigger condition is not finalized.

- Two or more tracks with $P_T > 300\mathrm{MeV}/c$ exist in the detector acceptance ($17^\circ < \theta < 150^\circ$).
- Total energy deposit exceeds a threshold value of $2\mathrm{GeV}/c$.

Table 5.1 shows estimated trigger rates for each event. With the final BELLE trigger system, a part of Bhabha events are identified and a large fraction of them is discarded.

Table 5.1: The estimated trigger rate for the typical events in the BELLE experiment.

Event	Cross Section (nb)	Trigger Rate (Hz)
$b\overline{b}$ Event	1.2	12
Continuum Event	2.8	28
Bhabha Event	44	440
$e^+ e^- \to \mu^+ \mu^-$ Process	0.8	8

In triggered 1,000,000 events we may have following counts of the events:

Table 5.2: The estimated number of the events for each event type in triggered 1,000,000 events.

Event	Number of Events
$b\overline{b}$ Event	2.5×10^4
Continuum Event	5.7×10^4
Bhabha Event	90×10^4
$e^+ e^- \to \mu^+ \mu^-$ Process	1.6×10^4

We have the following values to monitor:

- Number of the reconstructed tracks
- $\left|\sum \overrightarrow{P_T}\right|$
- $\left|\sum \overrightarrow{P}\right|$ in the laboratory frame and in the center of mass frame of $\Upsilon(4S)$
- $\sum \overrightarrow{P_z}$ in the laboratory frame
- $\sum \left|\overrightarrow{P}\right|$ in the center of mass frame of $\Upsilon(4S)$
- Maximum $\left|\overrightarrow{P}\right|$ value in the center of mass frame of $\Upsilon(4S)$

and for the event whose number of reconstructed tracks is two:

- Sum of the reconstructed charge
- Opening angle of the two tracks in the r-ϕ plane
- Opening angle of the two tracks in the volume

Number of triggered events for each event type is shown in Table 5.3.

Table 5.3: The number of triggered events.

Event	Triggered
$b\,\bar{b}$ Event	7829
Continuum Event	10000
Bhabha Event	5001438
$e^+\,e^- \to \mu^+\,\mu^-$ Process	49854

Both following figures and tables are not scaled by the total trigger rate for each event type.

5.1.1 Monitored Values for $b\,\overline{b}$ Events

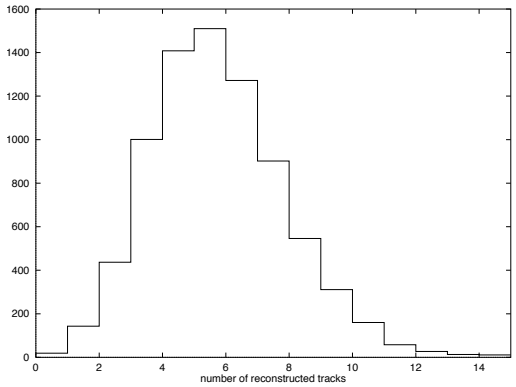

number of reconstructed tracks

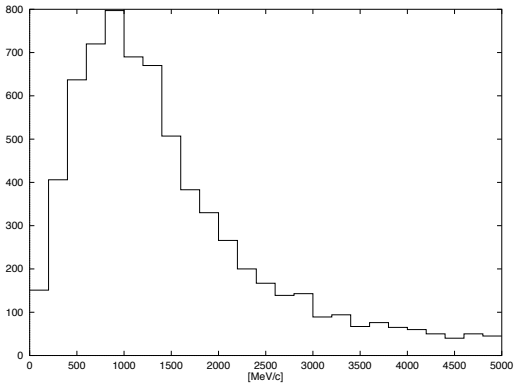

$\left|\sum \overrightarrow{P_T}\right|$

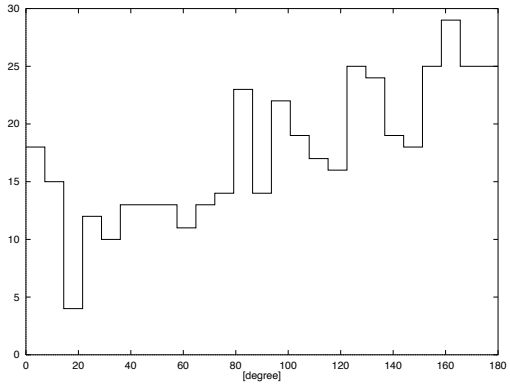

opening angle in r-ϕ plane for two track events

total charge for two track events

Total Charge	Number of Events
-2	71
0	238
+2	128

Figure 5.1: $b\,\overline{b}$ event reconstruction without z information

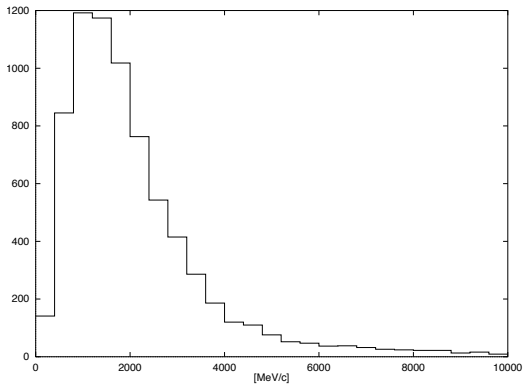

$\left|\sum \overrightarrow{P}\right|$ in the laboratory frame

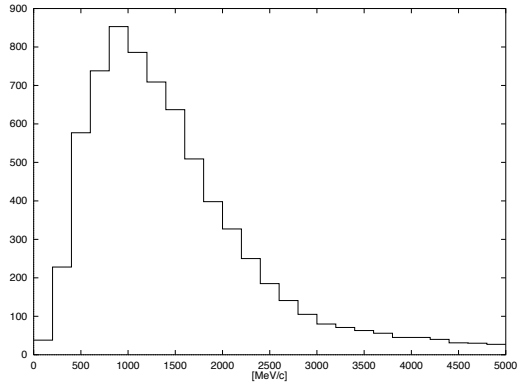

$\left|\sum \overrightarrow{P}\right|$ in the rest frame

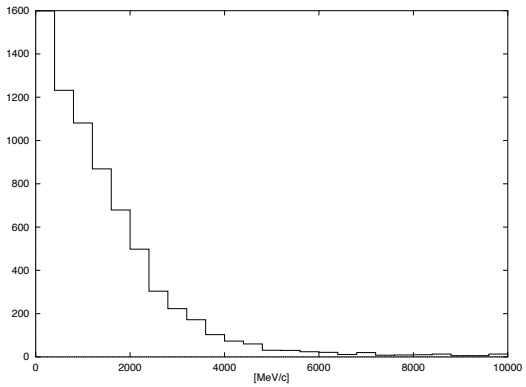

$\sum \overrightarrow{P_z}$ in the laboratory frame

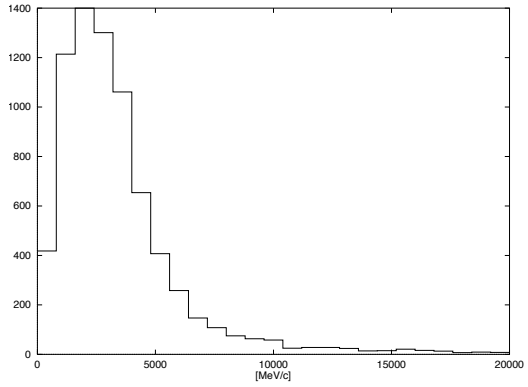

$\sum \left|\overrightarrow{P}\right|$ in the rest frame

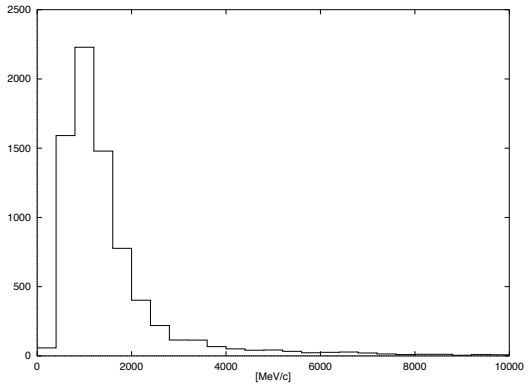

maximum of $\left|\overrightarrow{P}\right|$ in the rest frame

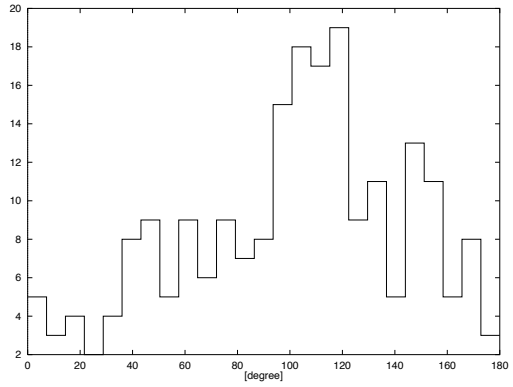

opening angle of in the volume for two track events

Figure 5.2: $b\,\overline{b}$ event reconstruction with z information

5.1.2 Monitored Values for Continuum Events

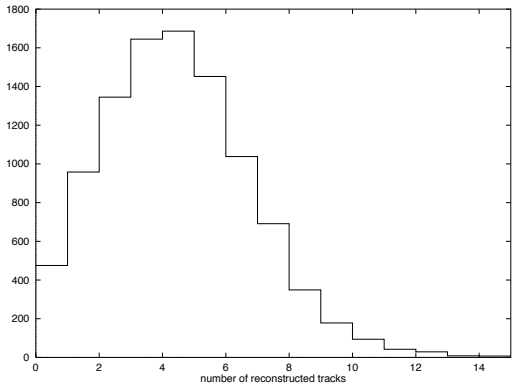

number of reconstructed tracks

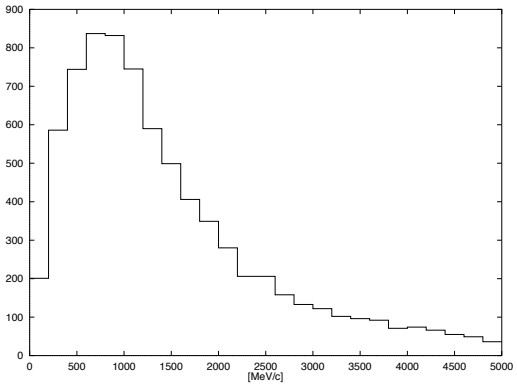

$\left|\sum \overrightarrow{P_T}\right|$

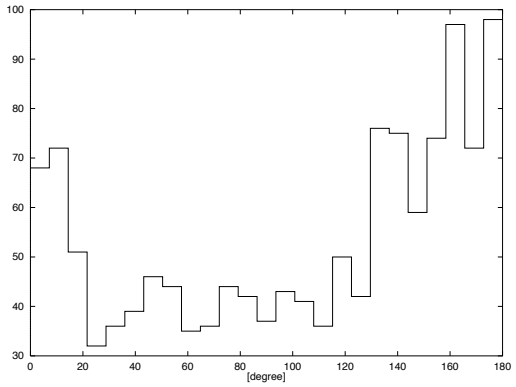

opening angle in r-ϕ plane for two track events

total charge for two track events

Total Charge	Number of Events
-2	168
0	820
+2	357

Figure 5.3: continuum event reconstruction without z information

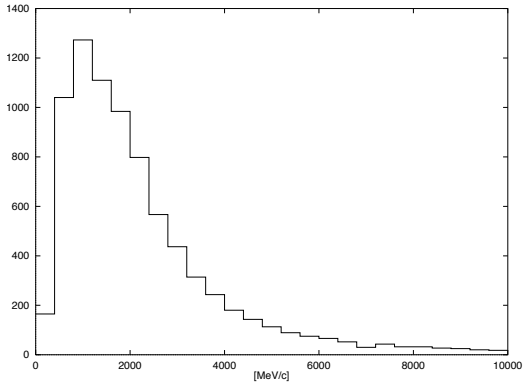

$\left|\sum \overrightarrow{P}\right|$ in the laboratory frame

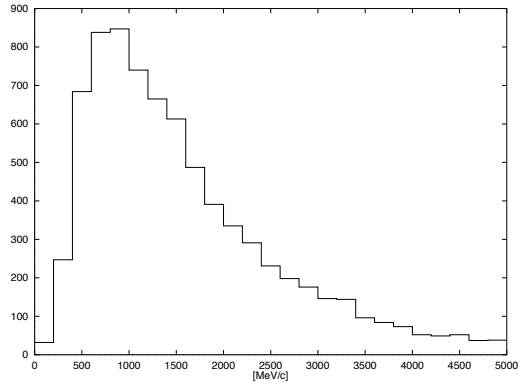

$\left|\sum \overrightarrow{P}\right|$ in the rest frame

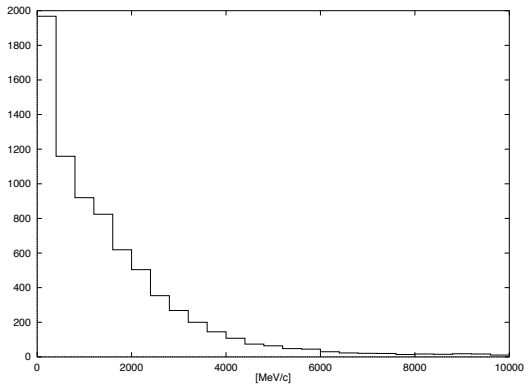

$\sum \overrightarrow{P_z}$ in the laboratory frame

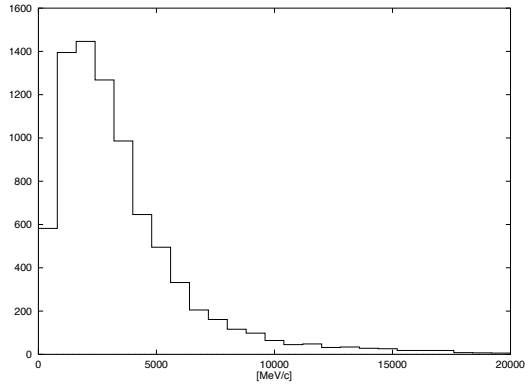

$\sum \left|\overrightarrow{P}\right|$ in the rest frame

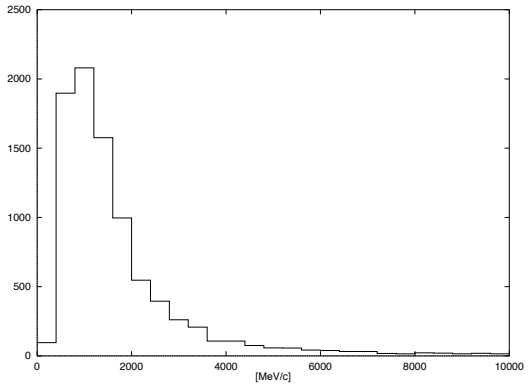

maximum of $\left|\overrightarrow{P}\right|$ in the rest frame

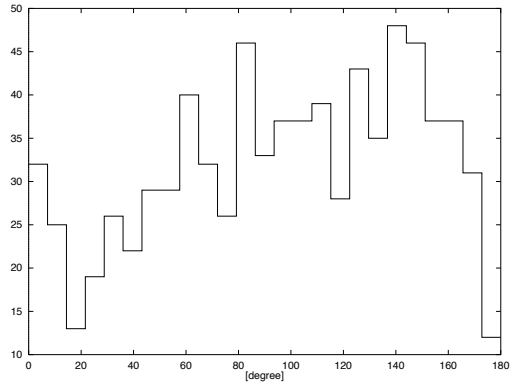

opening angle of in the volume for two track events

Figure 5.4: continuum event reconstruction with z information

5.1.3 Monitored Values for Bhabha Events

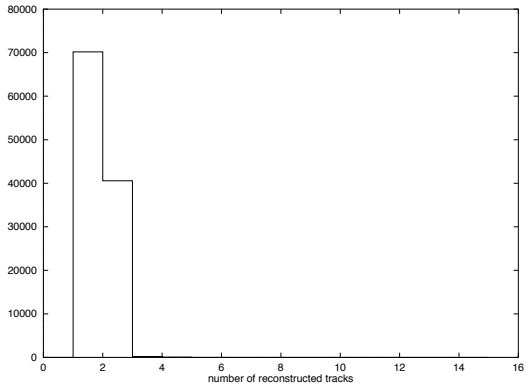

number of reconstructed tracks

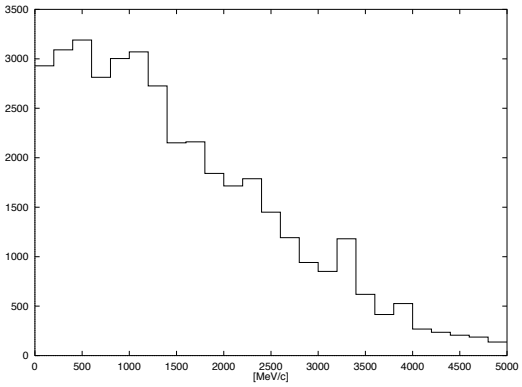

$\left|\sum \overrightarrow{P_T}\right|$

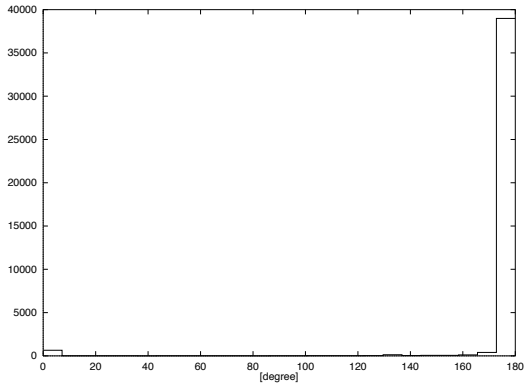

opening angle in r-ϕ plane for two track events

total charge for two track events

Total Charge	Number of Events
-2	25
0	40341
+2	206

Figure 5.5: Bhabha event reconstruction without z information

In Figure of 'number of reconstructed tracks', Bhabha events have 4,890,414 events with no reconstructed tracks because of it differential cross section. In the histogram $n = 0$ is not shown.

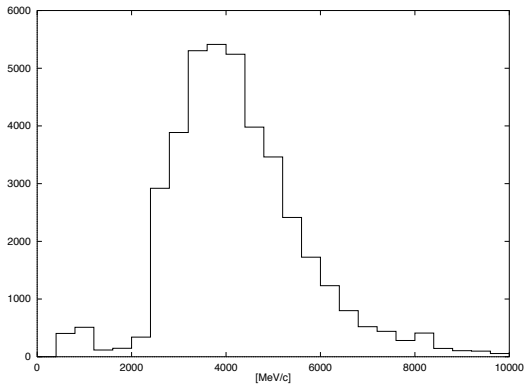

$\left|\sum \overrightarrow{P}\right|$ in the laboratory frame

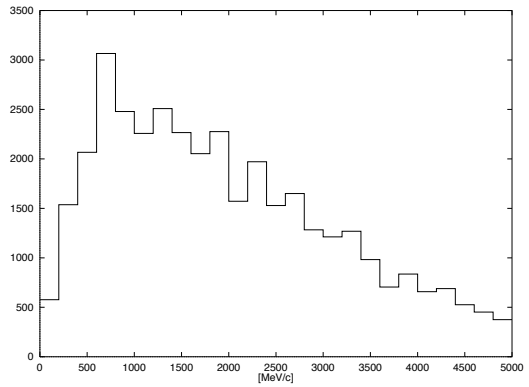

$\left|\sum \overrightarrow{P}\right|$ in the rest frame

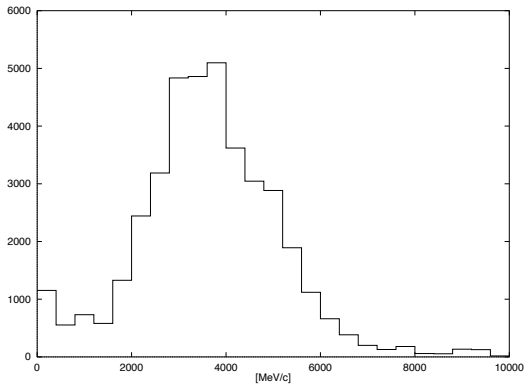

$\sum \overrightarrow{P_z}$ in the laboratory frame

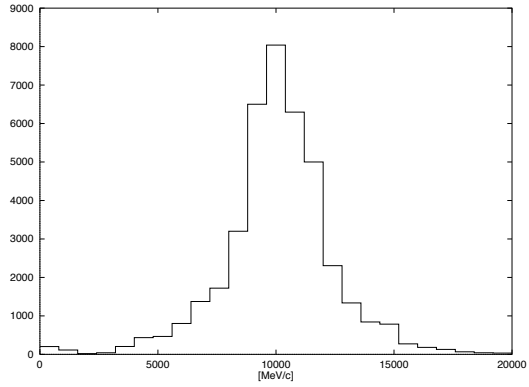

$\sum \left|\overrightarrow{P}\right|$ in the rest frame

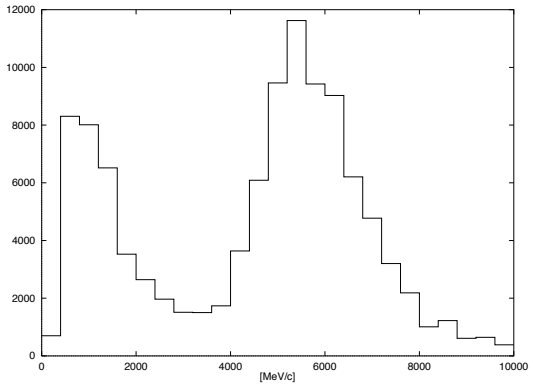

maximum of $\left|\overrightarrow{P}\right|$ in the rest frame

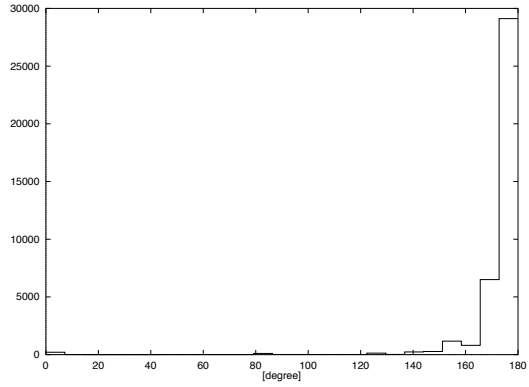

opening angle of in the volume for two track events

Figure 5.6: Bhabha event reconstruction with z information

5.1.4 Monitored Values for $e^+ e^- \to \mu^+ \mu^-$ Process

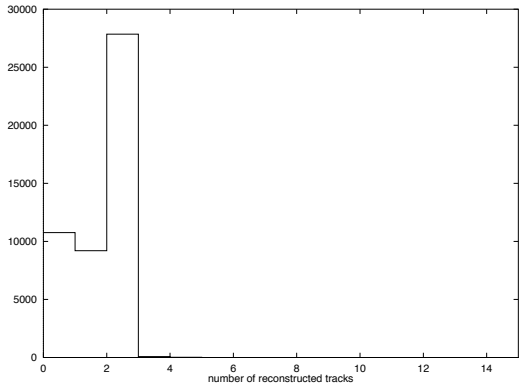

number of reconstructed tracks

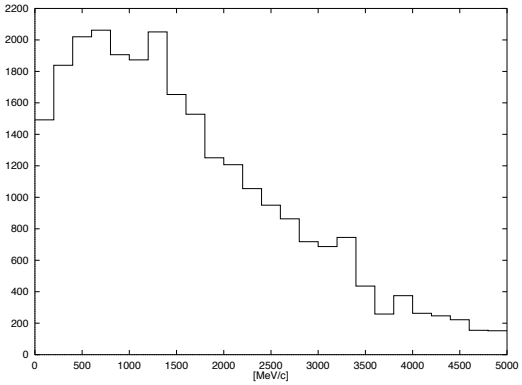

$\left|\sum \overrightarrow{P_T}\right|$

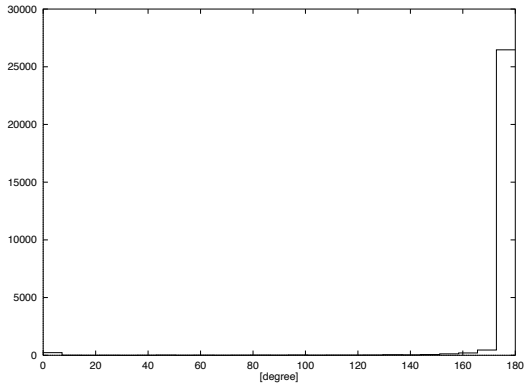

opening angle in r-ϕ plane for two track events

total charge for two track events

Total Charge	Number of Events
-2	25
0	27822
+2	2

Figure 5.7: $e^+ e^- \to \mu^+ \mu^-$ process reconstruction without z information

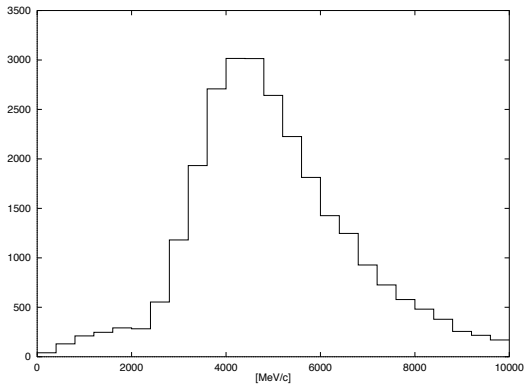

$\left|\sum \overrightarrow{P}\right|$ in the laboratory frame

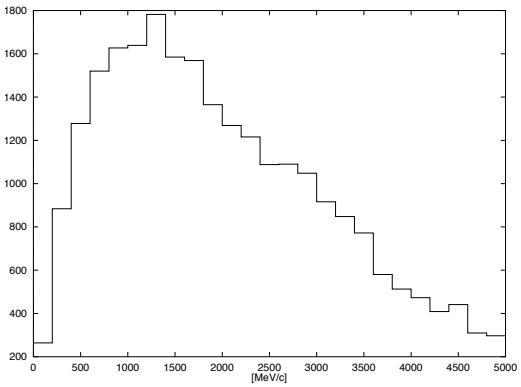

$\left|\sum \overrightarrow{P}\right|$ in the rest frame

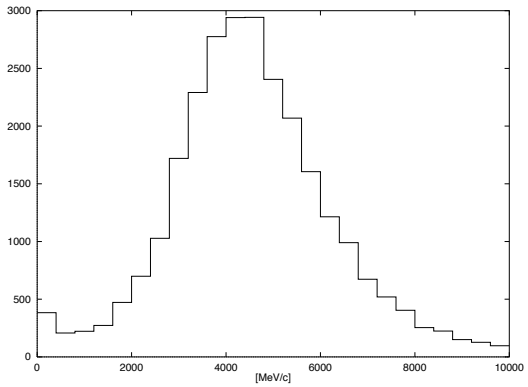

$\sum \overrightarrow{P_z}$ in the laboratory frame

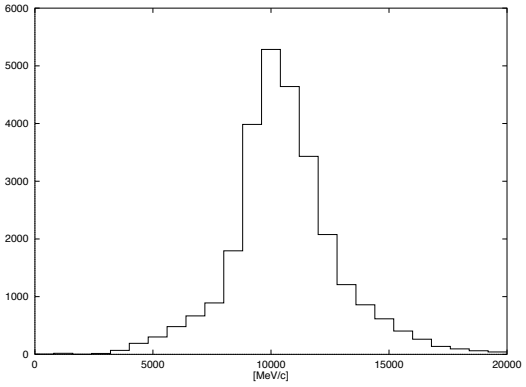

$\sum \left|\overrightarrow{P}\right|$ in the rest frame

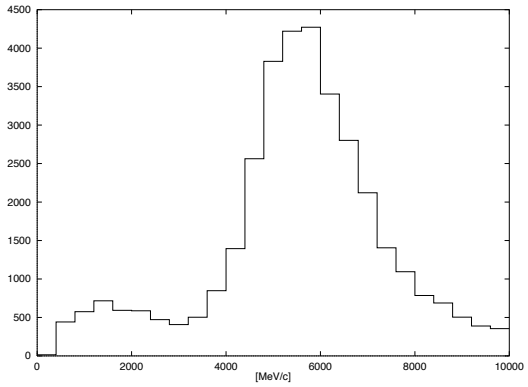

maximum of $\left|\overrightarrow{P}\right|$ in the rest frame

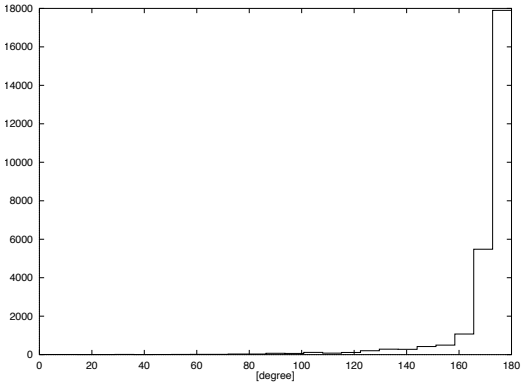

opening angle of in the volume for two track events

Figure 5.8: $e^+\,e^- \rightarrow \mu^+\,\mu^-$ process reconstruction with z information

5.2 Event Classification

Since the cross section of Bhabha events is very large, a large fraction of them must be discarded to save storage space and offline processing time. Event classification helps to achieve this. Event selection criteria are chosen to maximize the efficiency while keeping high purity.
Events are classified as either $b\overline{b}$ or continuum events (hadronic events) when one of the following criteria is satisfied.

- More than two tracks exist.
- When the number of reconstructed tracks is two, the total charge must be non-zero or the opening angle of tracks in the r-ϕ plane must be less than 178°.
- When only one track is reconstructed, $|P|$ must be less than 2GeV/c.

Events are classified as either leptonic events (Bhabha or $\mu^+\,\mu^-$) when one of following criteria is satisfied.

- When the number of the reconstructed tracks is two, total charge must be zero and opening angle of the tracks in the r-ϕ plane must be greater than 178°.
- When less than two track is reconstructed.

Table 5.4 shows the number of events classified as hadronic or leptonic for each event type. Note that a event can be classified as both hadronic and leptonic events so that the efficiency of classification is independent of selection criteria of other event type.

Table 5.4: The estimated efficiency of the event classification for each event type.

Event	Hadronic	Leptonic	Efficiency [%]
$b\overline{b}$ Event	7801	165	99.6
Continuum Event	9465	1449	94.7
Bhabha Event	33807	4997254	99.9
$e^+\,e^- \to \mu^+\,\mu^-$ Process	5596	44955	89.9

Although, the criterion of reconstructed track number = 0 is dominant for the leptonic event, for the hadronic event, especially $b\overline{b}$ event, we have good efficiency nearly 100%.

As for purity with scaling by the estimated trigger rate we have following results:

Table 5.5: The estimated result of the event classification for each event type.

Event	Purity [%]
Hadronic Event	90.3
Leptonic Event	99.1

We obtain the good result of hadronic event selection.

5.3 Processing Time

The elapsed time to process 300 $b\overline{b}$ events is measured to be 15.6s on one CPU. Since we have total of 120 CPUs, effective event processing time is 433μs per event. The number of tracks in $b\overline{b}$ events is larger than that of other event type. Therefore this result is considered to be the worst case. The processing speed is fast enough for maximum DAQ trigger rate of 500Hz.

Chapter 6

Summary

The event reconstruction program is developed to monitor the detector performance, to reject the background events, and to classify the events. The detector performance is monitored to identify any problem associated with detectors. The background events should be discarded as many as possible to save the storage space and to reduce the CPU time of the offline analysis. To withstand maximum DAQ rate of 500Hz, an event must be reconstructed within 2ms.

Track reconstruction is necessary to achieve above the goals. The track finding in the r-ϕ plane, r-ϕ momentum reconstruction and z momentum reconstruction are performed to reconstruct and obtain momenta of tracks. The track finding is performed based on memory lookup method using the r-ϕ trigger signals. The track momentum is reconstructed by fitting to a circle with linear approximation method using wire hit information. The z momentum is reconstructed by associating the r-ϕ track with z trigger information. Almost 100% of tracks with $P_T > 500\mathrm{MeV}/c$ are found. The momentum dependence of σ_{P_T}/P_T is parameterized to be $\sigma_{P_T}/P_T[\%] = 3.5 \times P_T[\mathrm{GeV}/c]$.

Various monitored values are shown as a result of event reconstruction. Hadronic and leptonic events are tagged using those monitored value. We have good event classification efficiency for the $b\overline{b}$ event nearly 100%, while the purity of hadronic event is kept more than 90%. The event reconstruction time per event is measured to be 433μs for $b\overline{b}$ event which satisfies the speed requirement.

Acknowledgments

First of all, I would like to express my great thank to the supervisor H. Aihara (Univ. of Tokyo).
R. Itoh (KEK) gave me the chance to address the online event processing and also gave me much advice through writing my thesis. I have no word to express my appreciation for him.
Y. Iwasaki (KEK), M. Tomoto (Univ. of Nagoya) and Y. Ushiroda (Univ. of Kyoto) thought me the detail of the trigger system. Without them my thesis might never be finished.
In the tracking, I asked many questions to H. Ozaki (KEK). He was really kind and helpful for me.
Finally I would like to appreciate greatly H. Tajima (Univ. of Tokyo).

Bibliography

[1] M. Kobayashi and T. Maskawa, Progr. Theor. Phys. **49**, 652 (1973)

[2] The BELLE collaboration, KEK Report 95-1, (1995)

[3] T. Higuchi, Proceedings of the International Conference on Computing in High Energy Physics, (1998)

[4] Christenson, J. H., J. Cornin, V. Fitch, ad R. Turlay, Phys. Rev. Lett. **13**, 138 (1964)

[5] N. Cabbibo, Phys. Rev. Lett. **10**, 531 (1963)

[6] Y. Ushiroda, Master Thesis, (1998)

[7] Thomas Joseph Killian, Master Thesis, (1978)

[8] M. Tomoto, Master Thesis, (1996)